High performance doped Li-rich $Li_{1+x}Mn_{2-x}O_4$ cathodes nanoparticles synthesized by facile, fast and efficient microwave-assisted hydrothermal route

Juliana B. Falqueto[1,2], Adam H. Clark[3], Aleš Štefančič[1], Glen J. Smales[4], Carlos A. F. Vaz[3], Albert J. Schuler[5], Nerilso Bocchi[2], Mario El Kazzi[1]*

[1] Electrochemistry Laboratory, Paul Scherrer Institute, CH-5232 Villigen PSI, Switzerland

[2] Federal University of São Carlos, Department of Chemistry, C.P. 676, 13560-970 São Carlos - SP, Brazil

[3] Swiss Light Source, Paul Scherrer Institute, CH-5232 Villigen PSI, Switzerland

[4] Bundesanstalt für Materialforschung und -prüfung (BAM), Unter den Eichen 87, DE-12205, Berlin, Germany

[5] Bioenergy and Catalysis Laboratory, Paul Scherrer Institute, Forschungsstrasse 111, 5232 Villigen PSI, Switzerland

ABSTRACT

Li-rich nanoparticles of $Li_{1+x}Mn_{2-x}O_4$ doped with Al, Co or Ni are successfully synthesized using a facile, fast and efficient microwave-assisted hydrothermal route. Synchrotron X-ray diffraction confirms the formation of crystalline cubic spinel phase type. X-ray absorption spectroscopy analysis at the Co and Ni K- and L-edges verify that the dopants are within the $Li_{1+x}Mn_{2-x}O_4$ spinel structure and are inactive during cycling in the bulk and at the surface. Moreover, we demonstrate that nanocrystallinity and cationic doping play an important role in improving the electrochemical performance with respect to $LiMn_2O_4$ microparticles. They significantly reduce the charge-transfer resistance, lower the 1st cycle irreversible capacity loss to 6%, and achieve a capacity retention between 85 and 90% after 380 cycles, with excellent columbic efficiency close to 99% without compromising the specific charge at 5C cycling rate. Furthermore, the Mn K- and L-edges attest that after long cycling the Mn oxidation state in the bulk differs from that of the surface caused by the Mn disproportion reaction; however, the cationic doping helps to mitigate the Mn dissolution with respect to the undoped $Li_{1+x}Mn_{2-x}O_4$ nanoparticles as indicated by inductively coupled plasma atomic emission spectrometer ICP.

INTRODUCTION

Lithium-ion batteries (LIBs) have proven to be the most efficient energy storage devices for portable electronics, electrical transportation, and as backup power, connected to the grid when electricity is produced from renewable sources. With the current generation of commercial LIBs, the anode and the cathode are based on host materials allowing for fast, reversible lithium-ion intercalation and (de-)intercalation, from/into the crystalline structure, over a wide voltage range. Generally, cathode materials are diverse, varying in transition metal composition and electrochemical performance.[1] The most common commercial high voltage cathode materials are layered oxides based on Ni and Co, frequently denoted as $LiNi_xCo_yMn_zO_2$ (NCM) and $LiNi_xCo_yAl_zO_2$ (NCA) families.[2] However, due to the high cost of Ni and Co, research on battery materials has changed focus towards the development of new cathode materials, based on safety, low cost and being abundant non-toxic materials.[3] Tarascon *et al*.[4] highlighted that greener and more sustainable batteries can be achieved by using cathode materials based on sustainable elements, such as Mn, and the subsequent replacement of high-temperature synthesis methods with lower-temperature alternatives, *e.g.* hydro(solvo)thermal synthesis and microwave-assisted processes.

In this context, $LiMn_2O_4$ cubic spinel type materials have shown great potential for LIB applications.[5] The cubic spinel type material can intercalate two lithium ions per unit cell, where one lithium ion is (de-)intercalated from/into the tetrahedral sites within the cutoff potential limits of 3.3 V and 4.3 V *vs.* Li^+/Li delivering a theoretical capacity of 148 mA h g^{-1} where the Mn oxidation state varies reversibly between 3.5+ and 4+.[6] It is worth mentioning that an oxidation state of 3.5+ for Mn corresponds to 50% of Mn in 3+ and 50% in 4+ oxidation state. However, it is well reported experimentally that when $LiMn_2O_4$ is cycled between 3.3 V and 4.3 V *vs.* Li^+/Li

it typically delivers an initial discharge specific capacity of around 120 mA h g^{-1}, while lower than its theoretical value, is acceptable if stable upon long cycling.[7] A second lithium ion is (de-)intercalated from/into the octahedral sites within the cutoff potentials limits of 2.0 V and 3.3 V *vs.* Li$^+$/Li delivering a theoretical capacity of 148 mA h g^{-1} [and 296 mA h g^{-1} as the theoretical capacity when cycled from 2.0 V until 4.3 V (de-)intercalating two lithium ions per unit cell] where the Mn oxidation state varies between 3+ and 3.5+. This low voltage window is not widely studied due to the unsatisfactory cyclability related to the strong presence of the irreversible Jahn-Teller distortion, leading to capacity loss upon cycling.[6] Another degradation mechanism proposed to cause an irreversible loss of capacity in LiMn$_2$O$_4$ is the slow dissolution of manganese at the electrode-electrolyte interface, according to the disproportion reaction $2Mn^{3+}_{(s)} \rightarrow Mn^{4+}_{(s)} + Mn^{2+}_{(slv)}$.[8] In order to mitigate the capacity fading and improve the cycling performance of LiMn$_2$O$_4$, some approaches have been suggested, including: (*i*) reducing the particle size to the nanoscale[9–12]; (*ii*) Li enrichment of the material (Li-rich LiMn$_2$O$_4$)[8,10,13] and (*iii*) partial substitution (1 to 3%) of Mn^{3+} by other cations[14–18], with these methods applied either separately or in combination.

Solid-state reactions are the most commonly used synthetic approaches to obtain the LiMn$_2$O$_4$ spinel type. In this method, high temperatures ($\geq$ 650 °C) are used to promote cation diffusion into the network of the precursors, although long synthesis times are required, as this diffusion process is kinetically slow. Furthermore, in many cases, micron-sized particles are obtained with a broad size distribution, different morphologies, and additional phases.[19] Alternative methods have been proposed with the goal of reducing the temperature and time of synthesis, as well as increasing morphological homogeneity and size control of products. In this sense, hydrothermal synthesis has proved to be capable of obtaining nano-sized LiMn$_2$O$_4$ where lower temperatures ($\leq$ 200 °C) and

using water soluble precursors. However, the majority of conventional heating methods (involving heat transfer by conduction or convection) still require long synthesis times and they can lead to inefficient and non-uniform reactions due to the formation of temperature gradients inside the reaction vessels.[20,21] Microwave-assisted hydrothermal/solvothermal synthesis methods have emerged as an alternative heating source to the conventional heating methods to reduce the reaction time[19] and provides a number of advantages when compared to other methods, such as: (i) uniform heating which leads to increased reaction speeds and significant energy savings; (ii) the absence of direct contact between the heat source and the reaction system (reagents and/or solvents); (iii) homogeneous nucleation leading to nano-sized particles with a narrow particle size distribution; (iv) excellent control of reaction parameters leading to higher quality of products, higher yields and increased reproducibility; (v) selective heating, if compounds present in the reaction mixture interact in different ways with microwaves.[19,22,23] Although, one challenge of this method is scale-up to industrial quantities of materials synthesized due to the limited penetration depth of microwaves. However, efforts on the scale up have already been reported and show promising results.[23–25]

Focusing on reducing the size of particles to the nanoscale, recent research using microwave-assisted hydrothermal synthesis to obtain nanomaterials has shown promising results in a variety of applications.[22] In particular, Ragupathy *et al.*[26] obtained undoped $LiMn_2O_4$ particles in the range of 100-200 nm by heating a suspension of amorphous MnO_2 in an aqueous solution of LiOH using a microwave reactor with a low temperature of 140 °C for 1 h. Another example is the work from Chen *et al.*[27], where undoped $LiMn_2O_4$ was obtained by conventional and microwave-assisted hydrothermal methods from $MnCl_2$, $KMnO_4$ and LiOH dissolved in water. The synthesis times and temperatures for the conventional method of synthesis varied from 1 to 18 hours at 150, 170

and 200 °C, while for microwave-assisted synthesis was performed for only 1 hour at 150 and 165°C. The materials synthesized by the microwave-assisted route showed improved electrochemical performance than those synthesized by a conventional hydrothermal route. Based on those promising results, in our study we took the next step to explore a facile, fast and efficient microwave-assisted hydrothermal route to obtain Li-rich $Li_{1+x}Mn_{2-x}O_4$ nanoparticles doped with small amounts (~1% to 2%) of Al, Co or Ni elements as cathode material for LIBs at low 140 °C and with extremely short reaction time of 5 min in order to further decrease the particle to the nanometer size.

EXPERIMENTAL PROCEDURES

Synthesis of the doped and nano-sized $Li_{1+x}Mn_{2-x}O_4$ spinels. $Li_{1+x}Mn_{2-x}O_4$ spinel doped, separately and individually, with Al, Co and Ni were successfully synthesized by the microwave-hydrothermal methodology. Water-soluble precursors were used throughout, namely: potassium permanganate ($KMnO_4$ Sigma-Aldrich, 99%) as source of Mn, lithium hydroxide ($LiOH.H_2O$ Sigma-Aldrich, 99%) as source of Li, acetone (Sigma-Aldrich, PA) as reducing agent for manganese (VII). Aluminum nitrate [$Al(NO_3)_3.9H_2O$ Sigma-Aldrich, 99.0%, cobalt nitrate [$Co(NO_3)_2.6H_2O$ Sigma-Aldrich, 99.0%] and nickel nitrate [$Ni(NO_3)_2.6H_2O$ Sigma-Aldrich, 98.5%] were used as cationic doping precursors. The mole ratio between Mn : Li : acetone was 1.0 $KMnO_4$: 1.2 LiOH : 1.1 acetone [21]; the mole ratio for Mn : doping was 1.00 $KMnO_4$: 0.050 Al^{3+} and 1.00 $KMnO_4$: 0.010 M^{2+} ($M^{2+} = Co^{2+}$ or Ni^{2+}). These values were based on the work from Liang *et al.*[28] and previous studies from Amaral *et al*. in Bocchi's group at the Federal University of São Carlos,[15] having found best results using 1 to 5% of doping. The ratios of Mn and Al, Co and Ni dopants are noted to be different. Preliminary studies identified that with the ratio of 1.000 Mn : 0.050 dopant, Co and Ni-doped spinel samples presented intense diffraction

peaks associated with their respective birnessite phases when using laboratory diffractometer with Cu Kα X-ray source (Figure S1 of Supporting Information). The same did not occur with the Al-doped spinel. For this reason, the ratio of Co and Ni dopants to 1 Mn : 0.010 dopant yielding an increased phase purity towards the spinel phase.

The synthesis of each $Li_{1+x}Mn_{2-x}O_4$ spinel (doped and undoped) was carried out in a microwave reactor (850 W) at 140 °C under constant magnetic stirring for 5 min. The doping process was carried out in the same reaction step as the synthesis of the $Li_{1+x}Mn_{2-x}O_4$ by addition of the respective aqueous cation nitrate precursor to the reaction vessel. The product was dried at 120 °C overnight and subsequently submitted to a treatment in an aqueous 0.1 mol L^{-1} LiOH solution into the same reactor at 140 °C under constant magnetic stirring for 10 min. This step is required to reduce the K^+ and increase the Li^+ contents in the spinel. Finally, the product was submitted to a heat treatment to achieve a suitable particles size for a better electrochemical response in a conventional microwave oven (800 W) for 4 min.[11] In total, undoped (used as reference) and three doped $Li_{1+x}Mn_{2-x}O_4$ spinel powders were obtained via microwave-hydrothermal synthesis, color labeled as undoped (black), Al-doped (blue), Co-doped (red) and Ni-doped (green).

Characterizations of the as-synthesized $Li_{1+x}Mn_{2-x}O_4$ and after different cycling states. Elemental analysis for Li, K, Mn, Al, Co and Ni was carried out using inductively coupled plasma atomic emission spectrometer (ICP-AES; Thermo Scientific iCAP6500 duo) to determine the chemical composition of the as-synthesized samples. The measurements were performed using the axial mode to probe the wavelengths of 460.2 nm for Li^+, 766.4 nm for K^+, 260.5 nm for Mn^{2+}, 309.2 nm for Al^{3+}, 238.9 nm for Co^{2+} and 231.6 nm for Ni^{2+}. Additionally, inductively coupled plasma optical emission spectrometry (ICP-OES, Spectro Arcos) was also used to determine the amount of Mn dissolved in the electrolyte and deposited on the Li metal anode counter electrode

after 200 cycles. The ICP-OES samples were prepared with then following procedures: cycled glass fiber separators were washed with 1.0 mL of DMC. These DMC solutions and the respective cycled Li metal anodes were dissolved into 3.0 mL of ultrapure water and 840.0 μL of HNO_3 (concentrated). The resulting transparent solution was subsequently diluted with ultrapure water before being subjected to ICP-OES analyses.

The morphology of spinel particles was analyzed by scanning electron microscopy (SEM) using a FEI Inspect F50 microscope, operating with 10 kV electron beam. Each spinel sample was dispersed in isopropanol with the aid of an ultrasonic bath for 15 min and, subsequently, the dispersions were drop cast on a silicon substrate.

Small-angle X-ray scattering (SAXS) measurements were performed at Bundesanstalt für Materialforschung und -prüfung (BAM), Germany, to confirm the size of spinel samples. These measurements were conducted using the MOUSE (Methodology Optimization for Ultrafine Structure Exploration) instrument, where X-rays are generated from microfocus X-ray tubes, followed by multilayer optics to parallelize and monochromatize the X-ray beams to wavelengths of Cu Kα (λ = 0.154 nm) and Mo Kα (λ = 0.711 nm).[29] The scattered radiation is detected on an in-vacuum Eiger 1M detector (Dectris, Switzerland), which was placed at multiple distances from the sample (between 55 - 2507 mm). The space between the start of the collimation up to the detector is a continuous, uninterrupted vacuum to reduce background. The powder samples were mounted on a flat sample holder, between two pieces of scotch magic tape. By using both photon energies over a range of overlapping sample-to-detector distances, a very wide range in scattering angle can be covered, and the fluorescence from the samples can be avoided. The resulting data have been processed and scaled to absolute intensity using the DAWN software package in a standardized complete 2D correction pipeline with uncertainty propagation.[30,31] The resulting

SAXS data were fitted and analyzed using McSAS, a Monte Carlo method to extract form-free size distributions.[32]

The samples were additionally characterized as-synthesized and after different cycling states at the Swiss Light Source (SLS) synchrotron, Switzerland, using soft and hard X-ray absorption spectroscopy (XAS) and X-ray diffraction (XRD). For that, the cells were stopped at different cutoff potentials then immediately disassembling in an Ar-filled glovebox. For some experiments, as mentioned below in the text, the stopped cells rested for 12 h at open circuit potential (OCP) prior disassembling. So, the cathode materials were systematically analyzed after distinct cycling states, namely: (*i*) 1st charge (delithiation) at 4.3 V *vs.* Li$^+$/Li, (*ii*) 1st discharge (lithiation) at 3.3 V *vs.* Li$^+$/Li, (*iii*) 1st discharge at 3.3 V *vs.* Li$^+$/Li + 12 h rest at OCP, (*iv*) 200 cycles + 12 h rest at OCP and (*v*) 350 cycles + 12 h rest at OCP. The long cycling states finished after completing a discharge at 3.3 V *vs.* Li$^+$/Li. The extracted cathodes were washed with dimethyl carbonate (DMC) to remove the residual salt and then divided in three parts. One part of the electrode was mounted on suitable sample holders for soft XAS characterization. The other remaining parts were removed from the Al current collector being one part directly loaded into a 0.3 mm diameter quartz capillary for powder XRD measurements and the other part mixed with cellulose in the ratio 4:50 for Mn K-edge and 25:50 for Co and Ni K-edges X-ray absorption near edge structure (XANES) loaded into 1.0 mm diameter quartz capillary.

The acquisition of Mn, Co and Ni L-edges XAS spectra in total electron yield (TEY) and total fluorescence yield modes (TFY) was carried out at the SIM beamline (SLS) with approximately 10 nm and 100s of nm depth analysis from the surface, respectively, by using soft X-rays in the range from 500 to 900 eV with flux ~10^{14} photons/s over a field of 25 μm. The secondary electrons

emitted by the sample as a function of photon energy were collected by measuring the electron current via a picoammeter (Keithley 6517B).

The XRD measurements were carried out at the MS beamline (SLS) using MYTHEN (Microstrip sYstem for Time-rEsolved experimeNts) solid-state silicon microstrip detector and wavelengths 0.5642403 nm and 0.5643284 nm (keeping the absorption coefficient μR below 1) in the range of $5° – 60°$.[33] The Rietveld refinements were performed with the TOPAS software package.[34] The hard XAS were performed at SuperXAS beamline (SLS) with a 2.9 T superbending magnet as the source.[35] The resulting beam was collimated using a Si coated mirror at 2.9 mrad and subsequently monochromatized using a channel-cut Si(111) crystal. The beam was focused on the sample to a spot size of 1 mm x 0.2 mm (H×V) using a Rh coated toroidal double focusing mirror. The spectra of Co and Ni K-edges were collected in step-scanning fluorescence detection mode using a 5-element SDD detector and Mn K-edge with quick scanning in transmission mode using 1 bar N_2 filled ion chambers. The data were processed using the ProQEXAFS software for energy calibration, normalization and data averaging.[36] Energy calibration was performed using, Co, Ni and Fe foils, respectively.

Electrode preparation and electrochemical evaluation. Cathodes were prepared from the synthesized materials and from a micron-sized $LiMn_2O_4$ spinel (labeled henceforward "micron-sized $LiMn_2O_4$" with color code pink), used as reference material. They were prepared by mixing the $LiMn_2O_4$ active material powders with conductive carbon (Super-C 65, Imerys) and polyvinylidene fluoride (PVdF, Arkema Kynar HSV 900), in a ratio of 80:10:10 wt%. N-methyl-2-pyrrolidone (NMP, Alfa Aesar) was used as a solvent to prepare homogeneous slurries, which were cast on Al foil (thickness of ~16 μm) and dried under dynamic vacuum at 80 °C overnight. Electrodes with a diameter of 13 mm were obtained by punching the dried coated slurries. A further

heating at 120 °C under dynamic vacuum was performed to remove the remaining water before inserting the electrodes in an Ar-filled glovebox. Half-cells were assembled using a commercial LP30 electrolyte [500 µL of 1 M $LiPF_6$ in 1:1 wt% ethylene carbonate (EC) and dimethyl carbonate (DMC), Gotion], glass fiber separator inserted between two Celgard 2400 separators and Li metal (Alfa Aesar, 0.75 mm thickness) as counter electrode. The resulting active material loadings for the cathode were ~4 mg cm^{-2}. Distinct electrochemical analyses were performed at room temperature. Cyclic voltammetry (CV) measurements were recorded by an multichannel VPM3, BioLogic Science Instruments using a scan rate of 0.1 mV s^{-1} in a voltage range of 3.3 and 4.3 V vs. Li$^+$/Li. Galvanostatic tests were performed in duplicate in the voltage range of 3.3 and 4.3 V vs. Li$^+$/Li using a BAT-SMALL system (Astrol Electronic with 100 channel capacity) in two conditions: (*i*) at constant rate of C/10 for long cycling test and (*ii*) from C/10 up to 5C rate for C-rate test (assuming the theoretical specific capacity of 1C = 148 mA h g^{-1} for that voltage range). Electrochemical impedance spectroscopy (EIS) measurements were also performed at OCP value before and after 350 cycles at fully discharge state using a multichannel (VPM3, BioLogic Science Instruments) over a frequency range of 300 kHz to 5 mHz with an amplitude of 10 mV root mean square (RMS) for sinusoidal. All the potentials reported thereafter are always given *vs.* Li$^+$/Li.

RESULTS AND DISCUSSION

Structure, composition and morphology of the as-synthesized Li$_{1+x}$Mn$_{2-x}$O$_4$. Figure 1A shows the XRD patterns using synchrotron X-ray radiation and obtained from the as-synthesized nanoparticles of Li$_{1+x}$Mn$_{2-x}$O$_4$. As indicated by the XRD patterns, all the spinels are highly crystalline. The diffraction patterns of undoped, Al-, Co- and Ni-doped Li$_{1+x}$Mn$_{2-x}$O$_4$ are all

similar, with diffraction peaks corresponding to the cubic spinel phase with space group $Fd\overline{3}m$ (ICSD-88644).[37] The presence of other phases associate with the dopants Al, Co or Ni and their impact on the crystallization were not detected. However, the samples presented a significant amount of a potassium birnessite type phase $K_{0.5}Mn_2O_{4.3}\cdot0.5H_2O$ with monoclinic structure and space group $C12/m1$ (ICSD-83236).[38] The potassium birnessite originates from the potassium permanganate used in the synthesis as water-soluble precursor source for Mn following the synthesis studies reported by Liddle *et al.*[21]. Another possible synthesis route to be explored in future studies for obtaining potassium free phase would be the use of the water-soluble lithium permanganate instead in the synthesis; although, $LiMnO_4$ is not thermally stable, violently decomposing to give MnO_2 and Li_2O and the hydrothermal decomposition of $LiMnO_4$ has been shown to produce a mix of layered and tunnel structure of oxides.[21]
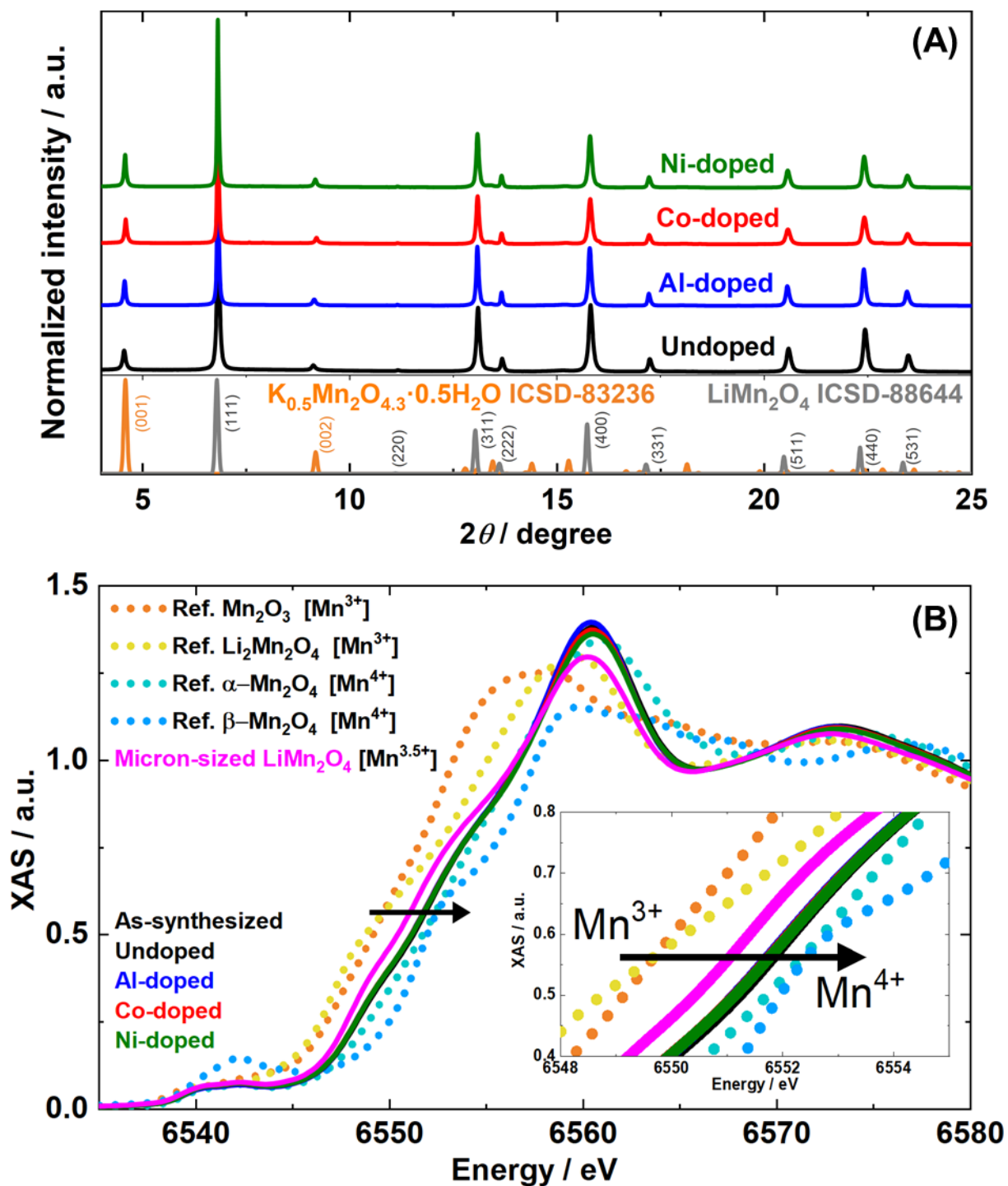
Figure 1. Results obtained from as-synthesized undoped, Al-, Co- and Ni-doped $Li_{1+x}Mn_{2-x}O_4$ spinels nanoparticles and reference materials: (A) experimental X-ray diffraction patterns, recorded using synchrotron radiation source and ICSD reference diffraction patterns of $LiMn_2O_4$

spinel type with cubic phase and $K_{0.5}Mn_2O_{4.3}\cdot0.5H_2O$ birnessite type with monoclinic structure; (B) Mn K-edge recorded in transmission mode. The horizontal black arrow located at an edge step of 0.563 represent the energy positions used to determine the mean Mn oxidation.

The chemical composition of the as-synthesized spinels was determined using ICP-AES with the contents of Li, K, Mn, Al, Co and Ni reported in Table 1. The O content was estimated based on the ICP-AES data and the oxidation state of the cations. For Li, K and Al, the oxidation states were fixed as 1+, 1+ and 3+, respectively. Table 1 also lists the (*i*) nominal mole ratio of Mn and doping precursors used in the syntheses, (*ii*) stoichiometric formulas, (*iii*) mean Mn oxidation states extracted from Mn K-edge X-ray absorption near edge structure (XANES) spectra (Figure 1B), (*iv*) particle size distribution width of the curves (derived from Monte Carlo fitting of the SAXS data, shown in Figure S2), and (*v*) unit-cell parameter *a* obtained from Rietveld refinement of the XRD data (Figure S4). In the case of Mn, the mean oxidation state was determined based on the position of the Mn K-edge XANES spectra (Figure 1B) when compared with known Mn reference materials (Figure S3). The mean oxidation states of Co and Ni were determined from Co and Ni K-edges by comparing with reference materials and are estimated to be ~2.7+ and ~2.0+, respectively (more details about the Ni and Co oxidation state will be provided later in the section "XAS, XRD and ICP analysis upon cycling"). The results confirm the doping of the as-synthesized spinels as being approximately 1% for Co and Ni and 2% for Al.

Table 1. Summary of the nominal mole ratio of Mn and doping precursors used in the syntheses, stoichiometric formulas, the mean Mn oxidation states determined from XANES spectra, and mean particle size and its distribution width for the as-synthesized nanoparticles of $Li_{1+x}Mn_{2-x}O_4$ spinels.

Samples	Mn and doping precursors ratio	Stoichiometric formula by ICP-AES	Mean Mn oxidation state by XANES	Mean particle size by SAXS / nm	Distribution width by SAXS / nm	Unit-cell parameter a / Å
Undoped		$Li_{1.15}K_{0.05}Mn_{1.79}O_{4.00}$	3.80 ± 0.05	61.2 ± 0.6	37.46	8.2022(1)
Al-doped	$1.000\ KMnO_4 : 0.050\ Al(NO_3)_3$	$Li_{1.37}K_{0.05}Al_{0.04}Mn_{1.75}O_{4.00}$	3.76 ± 0.05	92.0 ± 0.8	44.26	8.2148(4)
Co-doped	$1.000\ KMnO_4 : 0.010\ Co(NO_3)_2$	$Li_{1.31}K_{0.07}Co_{0.02}Mn_{1.78}O_{4.00}$	3.77 ± 0.05	107.0 ± 0.6	50.74	8.2095(2)
Ni-doped	$1.000\ KMnO_4 : 0.010\ Ni(NO_3)_2$	$Li_{1.22}K_{0.09}Ni_{0.02}Mn_{1.76}O_{4.00}$	3.78 ± 0.05	86 ± 1	41.54	8.2108(2)

Rietveld refinements of the XRD patterns obtain on the synthesized spinels reveal under-occupancy of Mn and a smaller unit-cell parameter than for a perfect spinel structure ($a = 8.241$ Å for stoichiometric $LiMn_2O_4$ from ICSD-88644), potentially indicating that all samples present excess of Li which substitutes onto the Mn site in the spinel structure. For the as-synthesized undoped spinel, 94.1(2)% occupancy of the Mn site (16d) was determined. Whereas, for Al-, Co- and Ni- doped samples 95.7(4)%, 95.5(3)% and 96.4(3)%, respectively was obtained. Although Li is almost invisible for hard X-ray techniques due to the low electron density, Rietveld analysis performed partially substituting of Mn by Li yielding unity site occupancy gave the best agreement with the experimental data. Furthermore, Li substitution of lattice Mn^{3+} increases the average oxidation state of Mn due to charge compensation (as indicated by XANES results in Table 1),[39] while also partly breaking the structural symmetry of the spinel acting as a structural pillar effectively reliving cell parameter change. Li substitution of lattice Mn^{3+} is noted to be beneficial in inhibiting irreversible phase transitions, like Jahn-Teller distortion, and, consequentially, the

capacity fade.[8] Another benefit of Li-rich spinel is the better diffusion of Li-ions through the structure because of the Li-excess configuration that introduces two types of fast Li-ion migration channels.[39]

Since particle size and surface morphology are important factors for the cycling performance, the as-synthesized nanoparticles of $Li_{1+x}Mn_{2-x}O_4$ were examined by both SAXS and SEM, respectively. The results from SAXS confirms the average size of the spinels, as shown in Figure 2C and reported in Table 1. It can be seen that all, as-synthesized $Li_{1+x}Mn_{2-x}O_4$, have somewhat developed octahedral morphologies with well-defined edges, indicating well-developed {111} planes.[40,41] In general, the morphology of the as-synthesized nano-spinels is very similar to those observed by other authors.[17,41,42] As such, it can be noted that spinel crystals with sharp edges were obtained under microwave hydrothermal conditions. The morphology of the particles, as observed by SEM, is similar for all samples. For comparison, the SEM image obtained for the micron-sized $LiMn_2O_4$ is also shown in Figure 2F which shows a very undefined morphology.
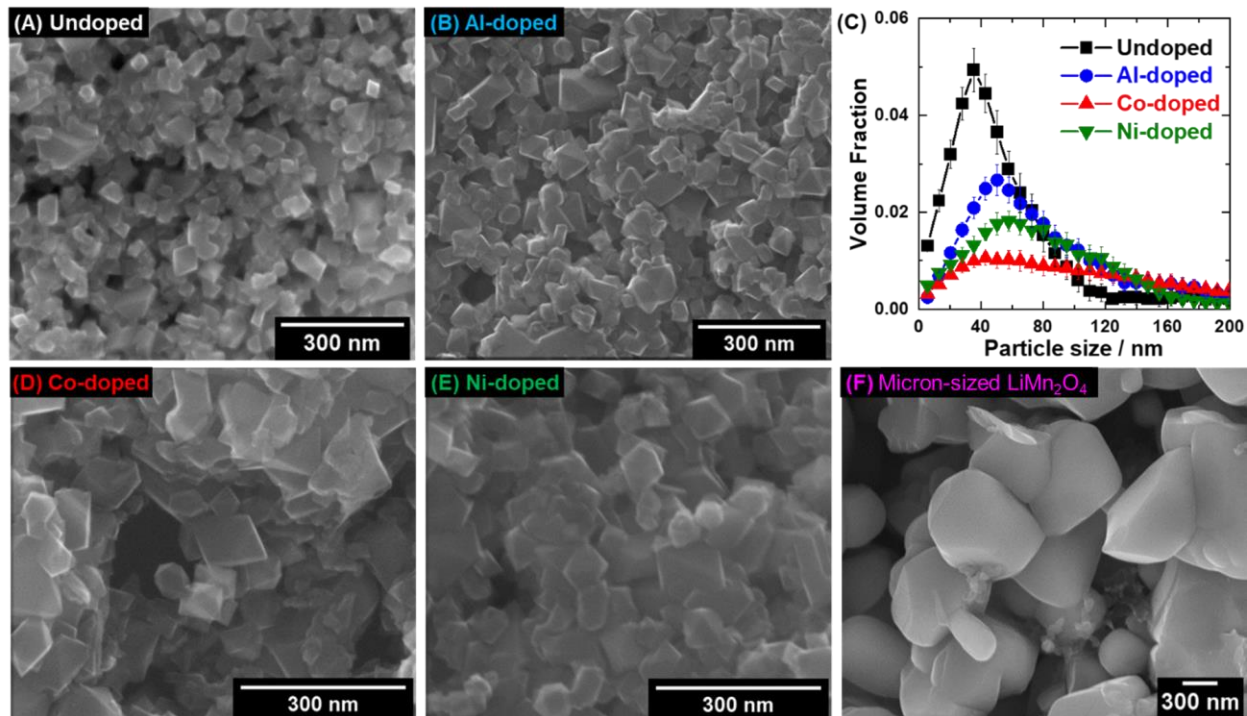
Figure 2. SEM images of as-synthesized (A) undoped, (B) Al-doped, (D) Co-doped, (E) Ni-doped $Li_{1+x}Mn_{2-x}O_4$ spinels nanoparticles obtained by the microwave-assisted hydrothermal route and (F) micron-sized $LiMn_2O_4$ spinel. In (C) the volume fraction distribution versus the mean particle size determined by SAXS for the as-synthesized $Li_{1+x}Mn_{2-x}O_4$ spinel nanoparticles.

The SAXS results indicate that the cationic doping process increases the particle size of the spinels. Comparing the values of mean particle size (Table 1) and their associated volume fractions (Figure 2C) among all synthesized $Li_{1+x}Mn_{2-x}O_4$, the undoped spinel presents the lowest average particle size (61.2 nm) and the narrowest particle size distribution, whereas the Co-doped spinel displays the largest average particle size (107.0 nm) and the widest particle size distribution. Al- and Ni-doped spinels have an average particle size around ~90 nm and comparable particle size distributions. The results obtained from the SAXS analysis compliment those obtained from SEM. Beside the increased particle size of the doped samples, no significant changes were observed among the four as-synthesized $Li_{1+x}Mn_{2-x}O_4$, indicating that the low doping with Al, Co or Ni (less

than 2.5%) had no significant effect on the surface morphology of the $Li_{1+x}Mn_{2-x}O_4$ nanoparticles synthesized by microwave hydrothermal methods.

Electrochemical cycling performance. In order to evaluate the influence of the cation doping and particle size on the electrochemical properties of the electrodes prepared from undoped and doped nano-sized $Li_{1+x}Mn_{2-x}O_4$, voltammetric, galvanostatic, and impedance measurements were performed. For comparison, electrodes prepared with the micron-sized $LiMn_2O_4$ were also tested. The CV profiles obtained for the electrodes prepared from all spinel electrodes are shown in Figure 3A. The curves display four peaks between 3.8 and 4.3 V which are typical of $Li_xMn_2O_4$, namely: (*i*) two anodic peaks (label with Ox) attributed to the oxidation process of Mn^{3+} to Mn^{4+} and, consequently, the Li^+ ions deintercalation from the spinel structure ($0 \leq x \leq 1$) and; (*ii*) two cathodic peaks (label with Rd) associated with the reduction of Mn^{4+} to Mn^{3+} and the consequent Li^+ ions intercalation within the structure. Both oxidation and reduction processes of Mn occur in two steps due to a redistribution of Li^+ ions in the tetrahedral 8a sites of the $Li_xMn_2O_4$, the first for $0 \leq x < 0.5$ and the second for $0.5 \leq x \leq 1$.[6] Comparing the CV profiles obtained for electrodes prepared from micron-sized $LiMn_2O_4$ and nano-sized (undoped and doped) $Li_{1+x}Mn_{2-x}O_4$ spinel, the first reveals well defined oxidation and reduction peaks at 4.04 and 4.17 V, and 4.10 and 3.97 V, respectively. The electrodes prepared from nano-sized materials also present broader, less pronounced and slightly shifted reversible redox peaks located at 4.07 and 4.18 V for the oxidation, and at 4.10 and 3.96 V for the reduction processes.
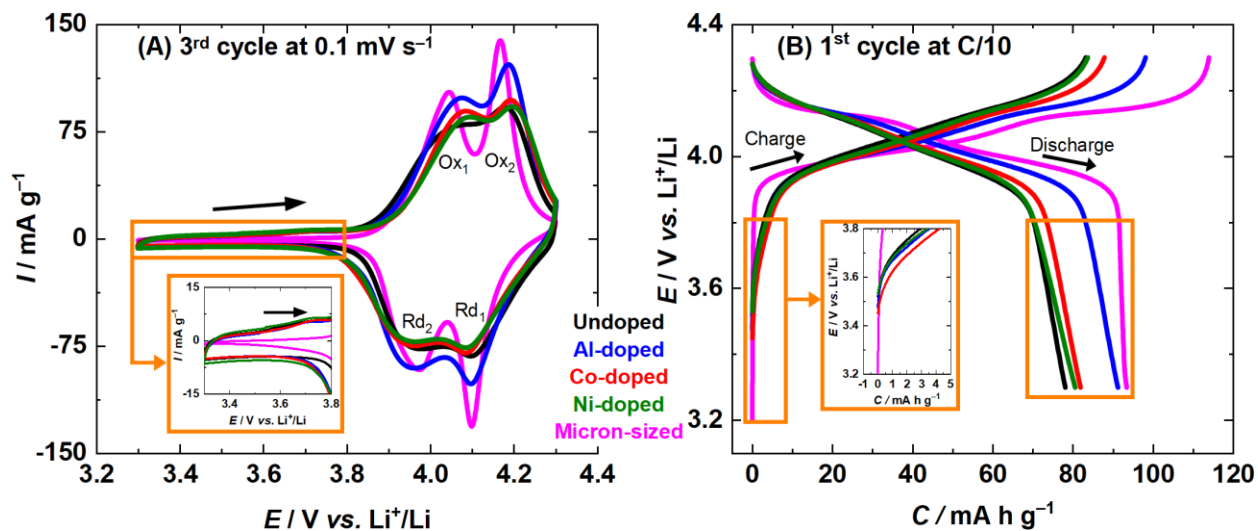
Figure 3. Electrochemical characterization obtained in half cell for electrodes prepared from undoped and doped nano-sized $Li_{1+x}Mn_{2-x}O_4$ spinels synthesized by the microwave-assisted hydrothermal route and from micron-sized $LiMn_2O_4$. (A) 3rd cycle of cyclic voltammetries at 0.1 mV s^{-1} (B) 1st cycle of galvanostatic charge-discharge test at C/10.

The galvanostatic tests performed at a C/10 rate are presented in Figure 3B. Typical profiles are observed with two plateaus associated with the same Mn oxidation (Li$^+$ ions deintercalation) and reduction (Li$^+$ ions intercalation) processes during charge and discharge, respectively. Cleary, the electrodes prepared from nano-sized synthetized $Li_{1+x}Mn_{2-x}O_4$ deliver lower apparent specific capacity than those prepared from micron-sized spinel in the first cycle. The low specific capacity is partially related to the presence of inactive potassium birnessite phase $K_{0.5}Mn_2O_{4.3}(H_2O)_{0.5}$ in the synthetized materials leading to an overestimation of the spinels active mass. The mass fraction of the active nano-sized synthetized $Li_{1+x}Mn_{2-x}O_4$ used in the cycled electrodes has been quantified from XRD data by Rietveld refinement (Figure S4) and reported in Table 2 together with the corrected specific capacity after removing the inactive birnessite contribution. The difference in the specific delivered capacity of the as-synthesized spinels with the micron-sized $LiMn_2O_4$ is less significant after the mass correction. It is worth mentioning that upon cycling, the XRD patterns

recorded on the undoped and doped $Li_{1+x}Mn_{2-x}O_4$ electrodes, the birnessite phase was no longer observed (Figure S5). This is thought to be due to dissolution of the potassium birnessite phase into the electrolyte. The effect of potassium from the birnessite dissolution on the electrolyte and on the surface of active material should be negligible due to the lower concentration of K^+ ions in the cell. This negligible effect is confirmed by the typical profiles obtained by cyclic voltammetry and galvanostatic curves of charge and discharge provided in the Figure 3. The concentration of K^+ ions in the electrolyte for the as-synthesized spinels are presented in the Table S5 and is far less than the concentration of the Li^+ ions in the electrolyte in the cells (1 mol L^{-1}). Additionally, the ionic radius of K^+ are significantly larger that Li^+ (1.38 Å vs. 0.76 Å),[43] which results in unfavorable conditions for the accommodation of the large K^+ ions into the spinel structure due to the higher (de-)intercalation energy than for the smaller Li^+ ions.

Table 2. Summary of the spinel percentage mass in the as-synthesized materials, specific capacities and coulombic efficiencies for 1st and 380th cycle before and after mass correction of the birnessite (quantified from XRD data by Rietveld refinement) and capacity retention for the synthesized and micron-sized spinels.

Spinel	Percentage of spinel / % (m/m)	Specific capacity before correction / mA h g^{-1}				Specific capacity after removing the birnessite contribution / mA h g^{-1}				Coulombic efficiency / %		Capacity retention after 380 cycles / %
		1st charge	1st disch.	380th charge	380th disch.	1st charge	1st disch.	380th charge	380th disch.	1st cycle	380th cycle	
Undoped	90.83(5)	81	76	70	69	89	**84**	77	76	94	99	91
Al-doped	89.0(9)	94	88	77	76	105	**99**	86	85	94	99	86
Co-doped	87.52(1)	85	80	73	72	97	**91**	83	82	94	99	90
Ni-doped	85.7(9)	85	81	70	69	99	**94**	82	80	95	99	85
Micron-sized	-	114	**94**	72	70	-	-	-	-	82	97	74

Another possible reason for the lower specific charge in nano-sized synthetized $Li_{1+x}Mn_{2-x}O_4$ can be related to the high surface area to bulk ratio of nanoparticles compared to micron-sized particles

[44–47]. Such behavior was previously observed for the same system by Miyamoto *et al.* (2015)[45] and for different cathode materials: TiO_2 by Wang *et al.* (2007)[46] and $LiCoO_2$ by Okubo *et al.*[44,47]. According to Okubo *et al.* (2007),[44] the site energy for Li^+ ions (de-)intercalation in bulk crystal can be assumed to be constant because there is no structural distortion or fluctuation, thus Li^+ ions (de-)intercalation is expected to take place at constant voltage. In nanoparticles, the Li^+ ions energy site for (de-)intercalation in the inner layers are equal to that in a bulk crystal, whilst, for the layers near the surface they are likely dispersive because of the distorted structure in the surface, which induces a fluctuation in the specific energy values for Li^+ (de-)intercalation. In the same work, the authors point out that the capacitor behavior became more dominant with decreasing crystallite size, while the plateau region at the voltage range 3.8 – 3.9 V (related to the capacity of the inner layers) decreases. This phenomenon also explains the less pronounced (broader) and slightly shifted in position redox couples peaks for the electrodes prepared from the nano-sized spinels observed in the CV profiles (Figure 3A).

Interestingly, as can be seen in Figure 3B and reported in Table 2, the synthetized nano-sized $Li_{1+x}Mn_{2-x}O_4$ electrodes have the higher 1st cycle coulombic efficiency in the range of 94% compared to the 82% for the micron-sized $LiMn_2O_4$. Furthermore, these results are superior to those typically obtained (~80%) by other authors for the 1st cycle.[16,17,48]

Figure 4 shows the electrochemical performance of the $Li_{1+x}Mn_{2-x}O_4$ electrodes after correcting the birnessite mass contribution. Figure 4A displays the values of specific discharge capacity and coulombic efficiency obtained over more than 380 charge/discharge cycles for electrodes prepared from undoped and doped nano-sized $Li_{1+x}Mn_{2-x}O_4$ spinel electrodes and from micron-sized $LiMn_2O_4$ (electrochemical performance of the cycled electrodes before correcting for the birnessite mass contribution is presented in Figure S8). The electrode prepared from micron-sized $LiMn_2O_4$

presents a rapid decay of the initial specific capacity as the cycle number increases, reaching a capacity retention of 74% after 380 cycles. Additionally, the coulombic efficiency for this material starts with a low value of 82%, reaching a maximum value of 98% at the 40th cycle and then slowly decreases to 97% by 380 cycles. All the nano-sized samples show a coulombic efficiency of 99% after 380 cycles and a capacity retention greater than 86% reported in Table 2, with the best result of 91% for the undoped nano-sized $Li_{1+x}Mn_{2-x}O_4$ presenting an excellent long-term stability. In terms of specific discharge capacity, the Al-doped nano-sized $Li_{1+x}Mn_{2-x}O_4$ delivered the highest value of 99 mA h g^{-1}, followed by Ni-doped, Co-doped and undoped nano-sized delivering 94, 91 and 84 mA h g^{-1}, respectively. The variation observed for the initial specific capacity values amount the doped spinels could be related to the differences from the cationic doping elements such as radius. Al presents the smallest radius (0.675 Å) among the doping elements and delivered the highest specific capacity, while Ni and Co present similar radius (~0.8 Å) and delivered similar values of specific capacity (radius values extracted from Shannon *et al.*[43]). This potentially induces small differences on the structure level even with small quantities of doping, generating better Li^+ diffusion paths and, consequently, better electrochemical performance. These electrochemical results corroborate with ICP and XRD results (Tables S1-S4), since Li-rich spinel contains structural defects that effectively suppress irreversible phase transformations during charge and discharge cycles, as a result, the cathode structural stability improves.
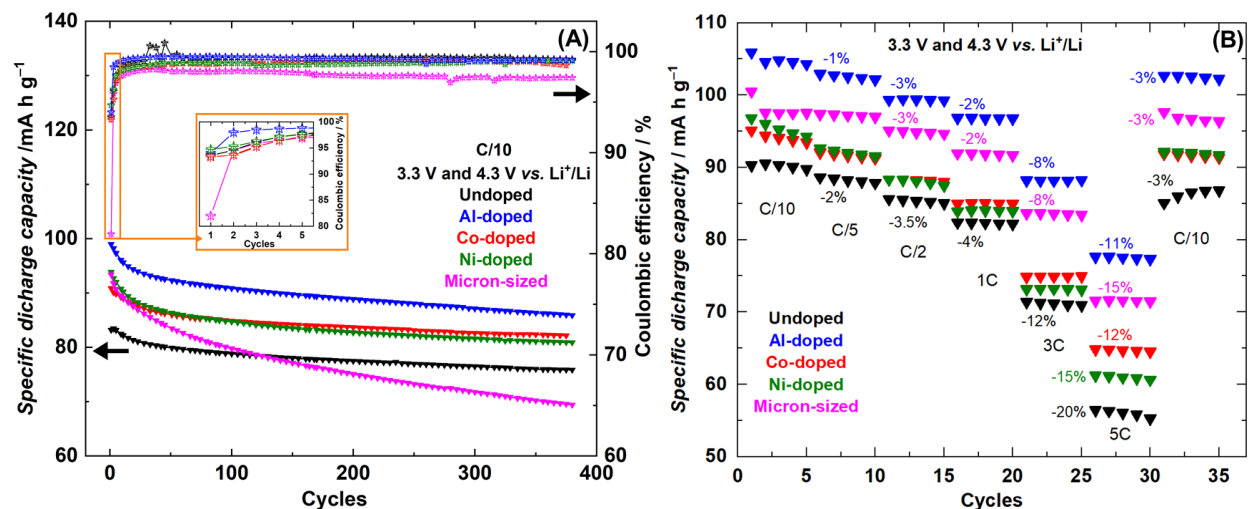
Figure 4. Electrochemical performance, after correcting for the birnessite mass contribution, of electrodes prepared from undoped and doped nano-sized $Li_{1+x}Mn_{2-x}O_4$ spinel samples synthesized by the microwave-assisted hydrothermal route and from micron-sized $LiMn_2O_4$ (A) at C/10 rate long-term cycling and (B) at different C-rates in half cell in the voltage range of 3.3 to 4.3 V.

Figure 4B shows the C-rates tests obtained for all cycles of the spinel electrodes. Figure S9 present the voltage profiles at the 1st cycle of each C-rate. As observed, the specific capacity decrease as the C-rates increase. For all electrodes, there is no significant difference in the specific capacity at C/10 and C/5 rates. By increasing the C-rate, the electrodes prepared from Al-doped and micron-sized spinels show the same percentage capacity loss (labeled in the Figure 4B), and a slightly lower loss when compared to the undoped, Co-doped and Ni-doped electrodes. At a higher rate of 5C, the doped nano-sized spinel electrodes presented a lower capacity loss compared to the undoped nano-sized with the Al doped spinel additionally outperforming the commercial micron-sized spinel. Furthermore, at 5C, the electrodes prepared from Al-, Co- and Ni-doped nano-sized spinels present superior specific discharge capacities (78, 65 and 61 mA h g^{-1}, respectively) to those typically achieved (~60 mA h g^{-1}) under the same experimental conditions reported elsewhere.[17,48] Finally, by comparing the initial and final specific capacity at C/10 rates it can be

23

inferred that all electrodes prepared from nano-sized $Li_{1+x}Mn_{2-x}O_4$ spinel synthesized by the microwave-assisted hydrothermal methods have excellent rate capability, presenting only a 3% loss of the initial capacity.

The OCP values measured before cycling for all spinel electrodes as well as the Mn mean oxidation state before and after 350 cycles are reported in Table 3. Before cycling, all electrodes prepared from undoped and doped nano-sized $Li_{1+x}Mn_{2-x}O_4$ spinel samples present an OCP values close to 3.51 V while those prepared from micron-sized $LiMn_2O_4$ presents an OCP value of 3.02 V. These results indicate that the Mn mean oxidation state in the structure of the nano-sized $Li_{1+x}Mn_{2-x}O_4$ is higher than that of micron-sized $LiMn_2O_4$, corroborating the XANES data in Table 1. The possible origins of the high Mn oxidation state of ~3.8+ for the uncycled nano-sized synthesized $Li_{1+x}Mn_{2-x}O_4$ electrodes compared to the 3.5+ for the micron-sized $LiMn_2O_4$ are the presence of the potassium birnessite phase $K_{0.5}Mn_2O_{4.3} \cdot (H_2O)_{0.5}$ having an average Mn oxidation state of ~4+, and the presence of excess Li which substitutes Mn^{3+} in the spinel structure leading to a higher average Mn oxidation state by charge compensation, as both reported above.[8] After the 1st discharge or 350th cycles, all the nano-sized synthesized $Li_{1+x}Mn_{2-x}O_4$ electrodes present an oxidation state close to the expected value of 3.5+ for the spinel. This behavior results from the dissolution of the potassium birnessite phase as confirmed by the XRD (Figure S5).

Table 3. Summary of the OCP and Mn mean oxidation state for all spinel electrodes before cycling, at the 1st charge at 4.3 V, 1st discharge at 3.3 V and after 350 cycles.

Spinel	OCP before cycling / V *	Mn mean oxidation state by XANES			
		Before cycling	1st charge	1st discharge	After 350 cycles
Undoped	3.50 ± 0.02	3.80 ± 0.05	3.92 ± 0.05	3.54 ± 0.04	3.39 ± 0.04

Al-doped	3.48 ± 0.02	3.76 ± 0.05	3.96 ± 0.05	3.57 ± 0.04	3.54 ± 0.04
Co-doped	3.52 ± 0.02	3.77 ± 0.05	3.88 ± 0.05	3.54 ± 0.04	3.40 ± 0.04
Ni-doped	3.53 ± 0.02	3.78 ± 0.05	3.89 ± 0.05	3.47 ± 0.04	3.39 ± 0.04
Micron-sized	3.02 ± 0.03	3.51 ± 0.04	3.98 ± 0.05	3.60 ± 0.05	3.56 ± 0.04

XAS, XRD and ICP analysis upon cycling. To gain further understanding of the cycling performance, XRD and XAS characterizations were performed on the spinel composite electrodes at different states of cycling. The oxidation state of Co and Ni in their respective as-synthesized $Li_{1+x}Mn_{2-x}O_4$ spinel and their possible contribution to the charge compensation upon (de-)lithiation were evaluated by performing hard XAS in fluorescence mode at the Co and Ni K-edges allowing to monitor the Co and Ni evolution in the bulk of the particles. Soft XAS at the Co and Ni L-edges have been also performed in TEY and TFY detection mode to monitor the Co and Ni changes on the surface and near surface of the particles. The oxidation state of both Co and Ni is found not to change significantly upon cycling, neither on the surface (Figure 5A, D and Figure S10) nor in the bulk (Figure 5 B and E), remaining at 2.7+ and 2.0+, respectively, as seen with the as-synthesized $Li_{1+x}Mn_{2-x}O_4$. Therefore, Co and Ni are proposed to not contribute to the charge compensation and specific capacity. In addition, Fourier transforms of the extended hard XAS spectra (Figure 5 C and F), may indicate that Co and Ni are incorporated into the structure of $Li_{1+x}Mn_{2-x}O_4$ spinels as seen by the shorter metal-metal distances observed in comparison to those observed for the respective oxide references (Co_3O_4 and NiO). The detailed analysis of the Ni and Co K-edge EXAFS, reported in Figure S11 and S12 and Table S6 and S7, indicate a metal-metal bond distance of 2.92 Å for both the Ni and Co local environments, corresponding to the expected distance for metal substitution into the spinel structure.
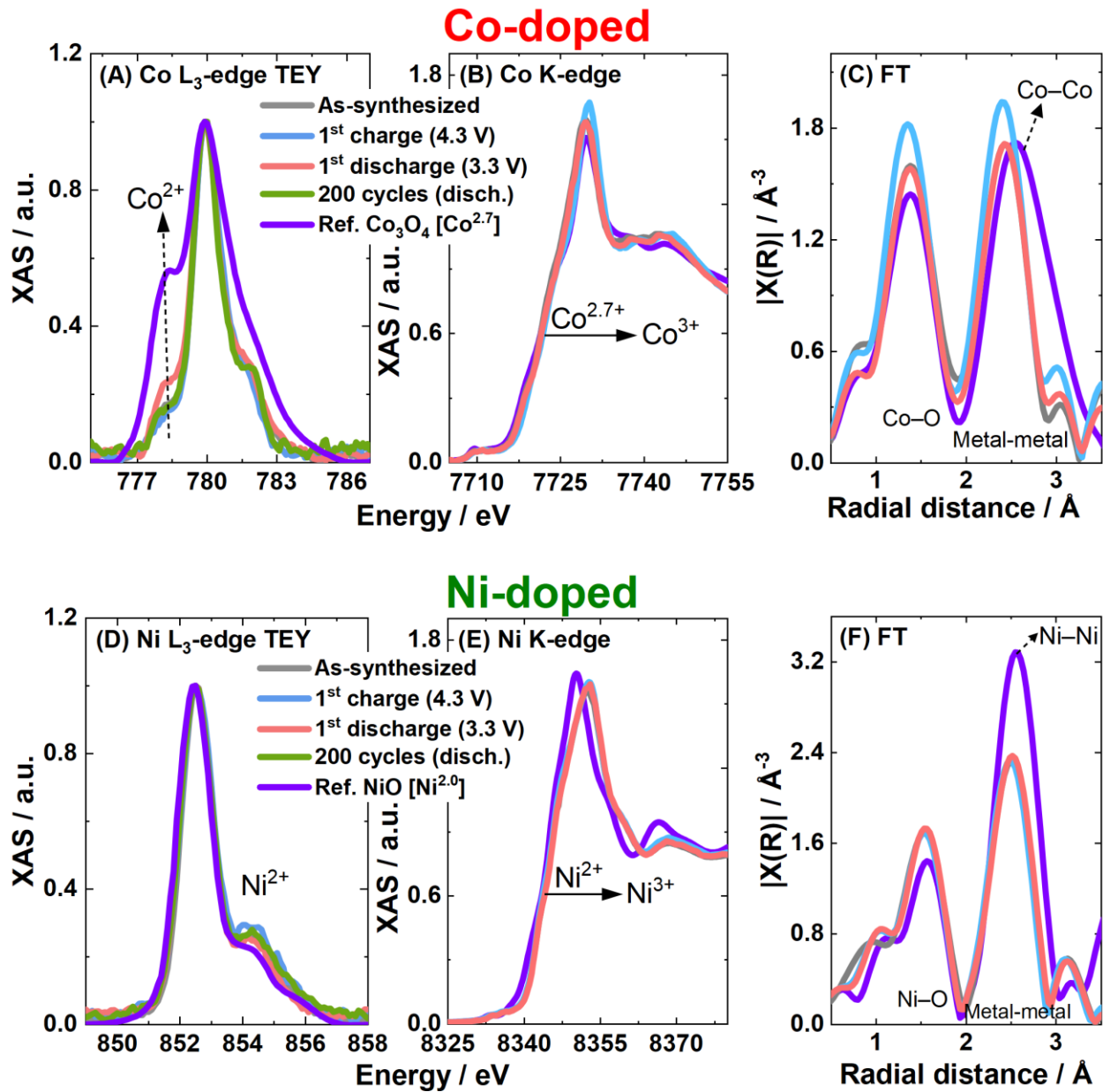
Figure 5. XAS measurements of Co- and Ni-doped $Li_{1+x}Mn_{2-x}O_4$ spinel electrodes collected in different cycling states at C/10 rate: 1st charge at 4.3 V *vs.* Li^+/Li, 1st discharge at 3.3 V *vs.* Li^+/Li and after 200 cycles (discharged state) compared with as-synthesized $Li_{1+x}Mn_{2-x}O_4$ and references materials Co_3O_4 and NiO. (A) Co and (D) Ni L-edges in TEY mode, (B) Co and (E) Ni K-edges in fluorescence mode and (C) and (F) Fourier transform (FT) result from Co and Ni K-edges, respectively.

In order to evaluate the changes in the Mn oxidation state in the bulk of the particles during charge and discharge, Mn K-edge spectra have been collected in transmission mode. The Mn K-edge of the as-synthesized and at different cycling states are presented in Figure 6 (close look in Figure S13). Each oxidation state was determined based on the position of the Mn K-edge XANES spectrum given in Table S8. The Mn K-edge spectra have been directly compared with reference materials of known Mn oxidation states, namely, Mn_2O_3 (Mn^{3+}), $Li_2Mn_2O_4$ (Mn^{3+}), $LiMn_2O_4$ ($Mn^{3.5+}$), α-Mn_2O_4 (Mn^{4+}) and β-Mn_2O_4 (Mn^{4+}). By comparing the values of Mn oxidation states calculated for the as-synthesized non-cycled electrodes (Figure 6E), we observe that the nano-sized $Li_{1+x}Mn_{2-x}O_4$ have a high Mn oxidation state of ~3.8+ instead of 3.5+ expected for pristine $LiMn_2O_4$ spinel and measured for the micron-sized $LiMn_2O_4$. As described above, this behavior is explained by the presence of inactive Mn^{4+} originating from the potassium birnessite phase $K_{0.5}Mn_2O_{4.3}(H_2O)_{0.5}$ and the presence of excess Li^+ which substitutes Mn^{3+} in the spinel structure.[8]

During the 1st charge (delithiation) the Mn in the micron-sized $LiMn_2O_4$ achieved a slightly higher oxidation state of 3.98+ compared to the nano-sized $Li_{1+x}Mn_{2-x}O_4$ (~3.9+, Table 3), which correlates well with the delivered specific capacities (Table 2). By comparing the Mn oxidation state and the delivered specific capacity between the different nano-sized synthetized $Li_{1+x}Mn_{2-x}O_4$, we confirm that the approach of Al doping is the most promising in facilitating the Li^+ ions extraction from the structure of the spinel, supported by the highest delivered specific capacity with the highest Mn oxidation state 3.96+ with respect to the undoped and Co and Ni doped $Li_{1+x}Mn_{2-x}O_4$ spinel.

During the 1st discharge (lithiation) the Mn oxidation state in the micron-sized $LiMn_2O_4$ is ~3.6+, higher than the 3.5+ measured on the non-cycled electrode. This result confirms the lower columbic efficiency of 82% achieved during the 1st cycle and the difficulty to reinsert Li^+ ions

back into the LiMn$_2$O$_4$ structure. Whilst the Mn oxidation state of the nano-sized Li$_{1+x}$Mn$_{2-x}$O$_4$ electrode is measured between 3.5+ (the lowest for Ni-doped), and 3.55+ (the highest for the Al-doped). In addition, this result demonstrates that the insertion of the Li$^+$ ions is much easier in the nanoparticles compared to the micron-sized particles which is also supported by the higher columbic efficiency ~94% during the 1st cycle achieved by the nano-sized particles.

Upon further cycling (200 and 350 cycles) stopped at the discharge (lithiation), it can also be noted that there is formation of excess Mn^{3+} for the undoped, Co-doped and Ni-doped Li$_{1+x}$Mn$_{2-x}$O$_4$ showing sequentially a decrease in the oxidation state to below the average expected value of Mn$^{3.5+}$. Synchrotron XRD measurements at the electrode after 200 cycles in the discharge state was performed to investigate if this excess of Mn^{3+} could be a sign of Jahn-Teller distortion (Figure S5). No peaks associated to the formation of the tetragonal distorted spinel phase, Li$_2$Mn$_2$O$_4$ with the space group $I41/amd$ (ICSD-40486),[49] were observed. This demonstrates that there was no significant formation of the crystalline Jahn-Teller phase in the nano-materials. However, from the XRD, it cannot be excluded that Jahn-Teller distorted Mn is not present in an amorphous phase.
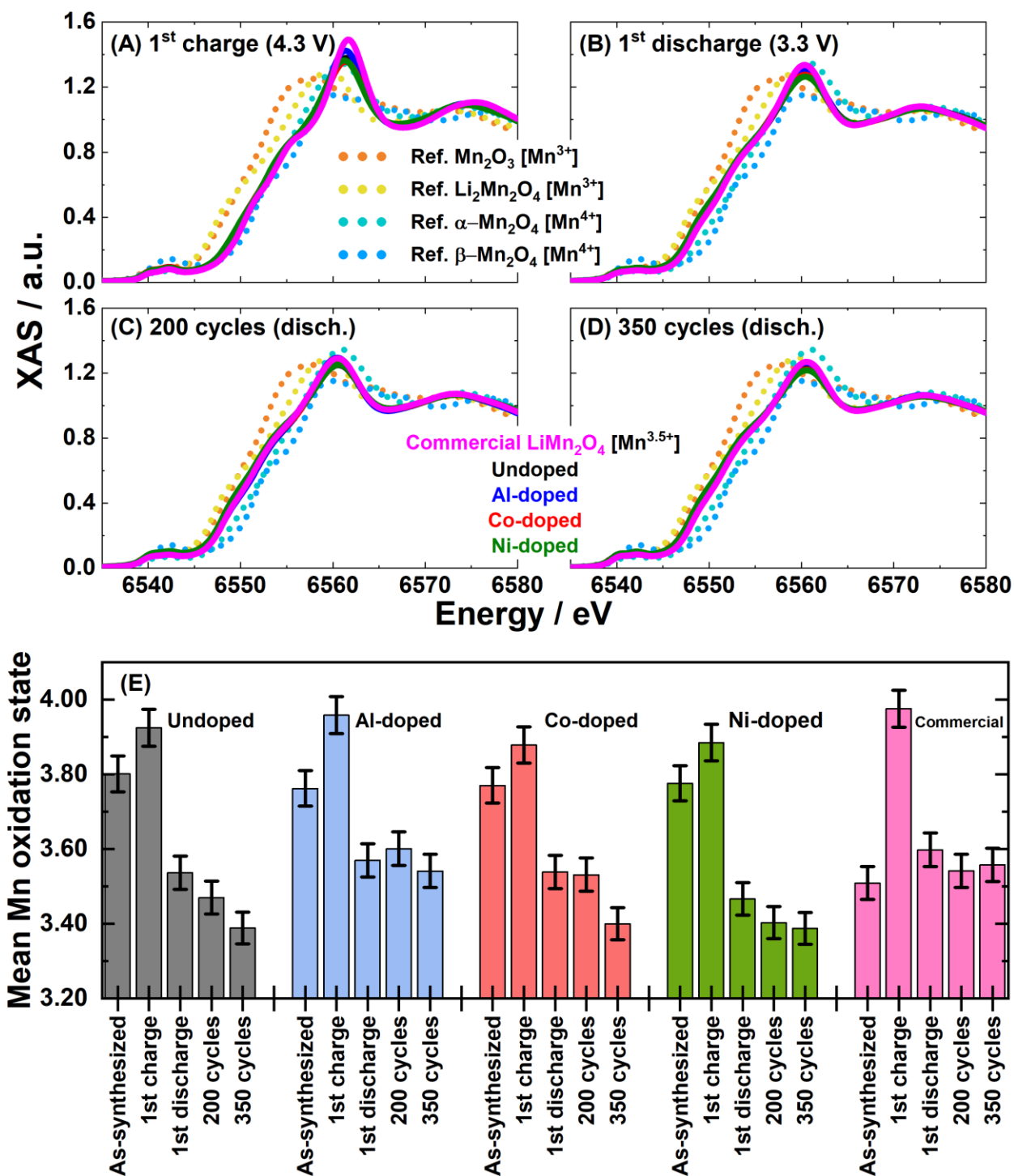
Figure 6. (A-D) Mn K-edge recorded in transmission mode and the (E) mean Mn oxidation state of as-synthesized, undoped, Al-, Co-, Ni-doped and micron-sized LiMn₂O₄ spinel electrodes in

different cycling states at C/10 rate: 1st charge at 4.3 V, 1st discharge at 3.3 V, 200 cycles in discharged state + 12 h of OCP (3.5 V) and 350 cycles in discharged state + 12 h of OCP (3.5 V).

With respect to the Mn oxidation state evolution on the surface of the spinel particles during charge and discharge, Mn L-edges spectra have been performed in TEY detection mode. The Mn L-edge spectra acquired on the as-synthesized and cycled electrodes stopped at different states are presented in Figure 7. Reference materials have been used to identify the Mn oxidation states features, such as $LiMn_2O_4$ where Mn is in both 3+ and 4+, $Li_2Mn_2O_4$ where Mn is in 3+, and fully delithiated micron-sized $LiMn_2O_4$ at 4.3 V representing Mn in 4+ (Figure 7F). As expected, the two features at ~642 eV and ~639.7 eV are associated with Mn^{3+} in $Li_2Mn_2O_4$, and features at ~643 eV and ~640.5 eV are associated with Mn^{+4} in the delithiated $LiMn_2O_4$. In the as-synthetized nano-sized $Li_{1+x}Mn_{2-x}O_4$ both Mn^{3+} and Mn^{4+} features are detected (Figure 7A). Qualitatively, the oxidation state of the Mn on the surface of the micron-sized $LiMn_2O_4$ is observed as being slightly more reduced in comparison to the nano-sized materials. This is visualized by the increase in intensity of the Mn^{3+} feature at approximately 642 eV of the micron-sized $LiMn_2O_4$. This behavior is again proposed to be caused by the presence of the potassium birnessite phase $K_{0.5}Mn_2O_{4.3}(H_2O)_{0.5}$ in the synthesized nano-sized $Li_{1+x}Mn_{2-x}O_4$ leading to an increase of the average Mn oxidation state, as demonstrated, by the Mn K edge XAS in Figure 1B and Table 1. During the 1st charge (delithiation) the Mn in the micron-sized $LiMn_2O_4$ shows a higher oxidation state compared to undoped and doped $Li_{1+x}Mn_{2-x}O_4$ spinels where the remanence of Mn^{3+} features are still visible (Figure 7B). This observation is in line with the results obtained above for the bulk of the spinel particles using the Mn K-edge (Figure 6). After the 1st discharge (lithiation), the Mn oxidation on the surface of all the spinel materials returns to a mixture of Mn 4+ and 3+ (Figure 7C). However, the micron-sized $LiMn_2O_4$ sample shows the highest degree of Mn^{3+} on the surface,

which is in sharp contrast when compared to the bulk, where the Mn shows the highest oxidation state of 3.6+ compared to the nano-sized $Li_{1+x}Mn_{2-x}O_4$ (Figure 6). During long cycling (200 and 350 cycles Figure 7D and E respectively), the surface composition does not evolve much with approximately the same ratio between the Mn^{3+} and Mn^{4+} detected as compared to the 1st discharge. This behavior is in contradiction with the Mn oxidation state detected in the bulk of the spinel particles where undoped, Co and Ni-doped nano-sized $Li_{1+x}Mn_{2-x}O_4$ show a significant decrease in the Mn average oxidation state close to 3.4+ (Figure 6). These observations demonstrate that the Mn oxidation state on the surface do not always follow that from the bulk of the particles, in particular for the discharged state. This behavior is well known in high voltage cathode materials, especially with $LiMn_2O_4$ particles, where surface structural reconstruction and dissolution process of transition metal is most likely to take place.[50,51]
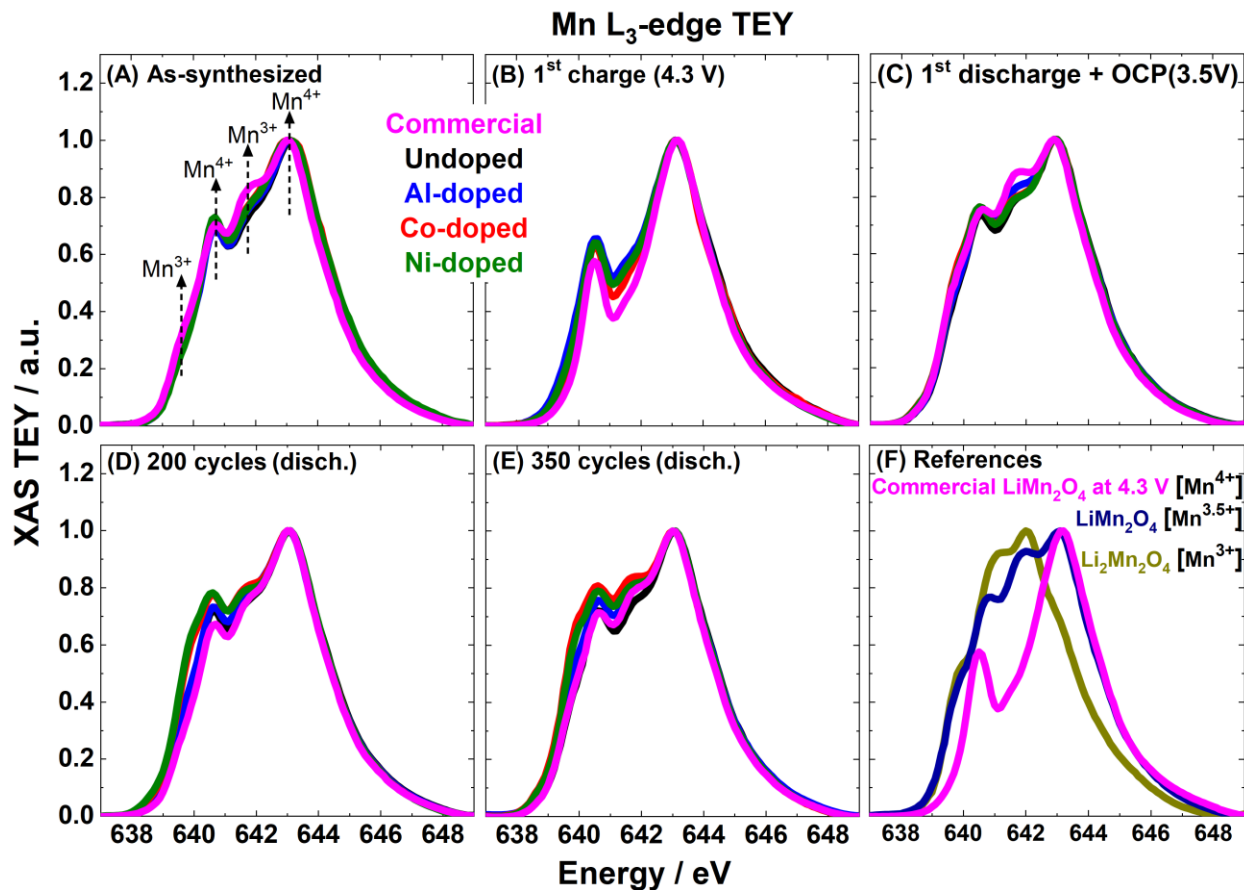
Figure 7. Mn L-edge, recorded in TEY mode, obtained from $Li_{1+x}Mn_{2-x}O_4$ spinel electrodes (A) as-synthesized and at different cycling states at C/10 rate: (B) 1st charge at 4.3 V, (C) 1st discharge at 3.3 V + 12 h of OCP (3.5 V), (D) 200 cycles in discharged state + 12 h of OCP (3.5 V), (E) 350 cycles in discharged state + 12 h of OCP (3.5 V) and (F) references materials.

The structural evolution of the synthesized $Li_{1+x}Mn_{2-x}O_4$ spinel cathodes upon charge/discharge processes and long cycling was investigated by XRD using synchrotron X-ray (Figure S5 and S6). Structural variation in the lattice parameter *a* can be seem in Figure S7. Upon delithiation (1st charge), the lattice parameter contracts and, during lithiation (1st discharge), expands back recovering to the original place. After the 200 cycles, no significant change in the lattice was

observed. The nano-sized $Li_{1+x}Mn_{2-x}O_4$ spinels synthesized by the microwave-assisted hydrothermal route present upon cycling an enhanced stability of the lattice parameter values.

To investigate the degree of Mn dissolution, ICP-OES was used to quantify the amount of Mn dissolved in the electrolyte and deposited on the Li metal anode after 200 cycles (Table S11). The concentration of Mn for the nano-sized undoped spinel reaches 1.21 mg L^{-1} whilst for Al-doped, Co-doped and Ni-doped the amount of the dissolved Mn is 0.616, 0.651 and 0.804 mg L^{-1}, respectively. Therefore, it is proposed that the cationic doping helps to mitigate the Mn dissolution from the nano-sized spinel even after considering the dissolution of the potassium birnessite present in the synthetized nano-sized $Li_{1+x}Mn_{2-x}O_4$. In support of this, it is noted that the synthesized undoped spinel presented the lowest percentage of potassium birnessite phase [9.16(5)% $^m/_m$] (Table S5) and has the highest value of Mn concentration deposited on the Li metal anode. More details can be found in the Figure S16 and Table S11.

Impedance spectroscopy. To further study the electrochemical behavior of the $Li_{1+x}Mn_{2-x}O_4$ spinels, EIS measurements were conducted in electrodes prepared from undoped and doped nano-sized $Li_{1+x}Mn_{2-x}O_4$ spinel samples and from micron-sized $LiMn_2O_4$ at OCP before and after 350 cycles at C/10 rate at fully discharge state (Figure 8). In general, all spectra consist of a singular or two depressed semicircles in the high-to-medium-frequency regions and an almost straight line in the low frequency regions in good agreement with those reported by Wood et al..[52] The high-frequency intercept at real axis corresponds to the ohmic resistance caused by the electrolyte. Low values of electrolyte resistance before and after cycling were observed owing to the cell geometry employed in the EIS measurements. According to Wood et al.,[52] the medium-frequency region represents the charge-transfer processes, both from electrolyte to the electrodes surface and from the electrodes surface to the bulk active material of the electrodes. The charge-transfer processes

(or charge-transfer resistance, R_{CT}) is an indication of the kinetic of the ion transport. The low-frequency region represents the diffusion process of the Li-ions in the electrodes.[52] As can be seen in Figure 8A, all spinel electrodes present a singular depressed semicircle before cycling. The electrodes prepared from nano-sized $Li_{1+x}Mn_{2-x}O_4$ spinels have smaller semicircles than those prepared from micron-sized $LiMn_2O_4$. After 350 cycles in the discharge state, the electrode prepared from micron-sized $LiMn_2O_4$ has clearly two depressed semicircles being: a first more defined with its center around 100 Ω and a second whose center is around 300 Ω (Figure 8B). Comparing this spectrum with those obtained for electrodes prepared from nano-sized $Li_{1+x}Mn_{2-x}O_4$ spinels, the first depressed semicircle obtained for the electrode prepared from micron-sized $LiMn_2O_4$ is more than twice as large than the semicircles obtained for electrodes prepared from nano-sized $Li_{1+x}Mn_{2-x}O_4$ spinels.
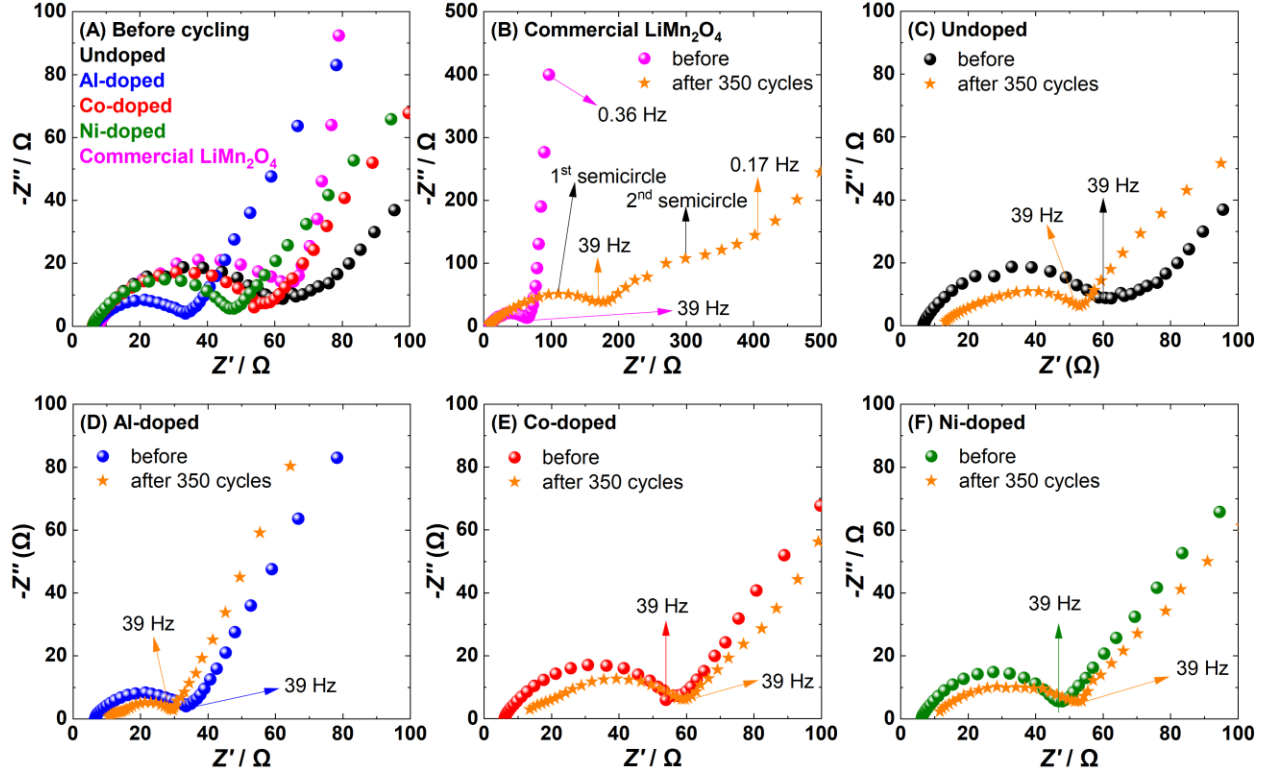
Figure 8. (A) EIS spectra acquired at OCP before cycling for electrodes prepared from spinels samples in the frequency range of 300 kHz to 5 mHz with an amplitude of sinusoidal voltage of 10 mV (rms). EIS spectra acquired at OCP before (sphere) and after 350 cycles at C/10 rate (star) in the fully discharge state for electrodes prepared from (B) micron-sized $LiMn_2O_4$, and nano-sized $Li_{1+x}Mn_{2-x}O_4$ spinel samples: (C) undoped, (D) Al-doped, (E) Co-doped and (F) Ni-doped. The galvanostatic cycling was performed in the voltage range of 3.3 to 4.3 V.

Typical EIS spectra acquired at OCP before (sphere) and after 350 cycles (star) at C/10 rate in the frequency range of 300 kHz to 5 mHz with an amplitude of sinusoidal voltage of 10 mV (rms) for electrodes prepared from undoped and doped nano-sized $Li_{1+x}Mn_{2-x}O_4$ spinel samples and from micron-sized $LiMn_2O_4$. The galvanostatic cycling was performed in the voltage range of 3.3 to 4.3 V.

From this result, it can be inferred that the R_{CT} value is higher for micron-sized $LiMn_2O_4$ than that for nano-sized spinels. It is important to note that while the EIS spectra was acquired at distinct OCP values (Table S12), they can still be compared since all OCP values are in the range of 3.0 to 3.8 V in which there is no significant redox process as shown by the CV and the charge-discharge profiles in Figure 3 (insets). Taking into account this consideration, the EIS results are in agreement with those obtained from long cycling tests (Figure 4A), *i.e.*, the nano-sized $Li_{1+x}Mn_{2-x}O_4$ spinel synthesized by the microwave-assisted hydrothermal route show better cycling stability than the micron-sized $LiMn_2O_4$. Nanocrystallinity and cationic doping, in particular with Al, was seen to play an important role in the improvement of the charge-transfer resistance.

CONCLUSIONS

Li-rich $Li_{1+x}Mn_{2-x}O_4$ spinel nanoparticles doped with Al or Co or Ni were successfully synthesized using a facile, fast and efficient microwave-assisted hydrothermal route. Moreover, nanocrystallinity and cationic doping were shown to play an important role in the improvement of the electrochemical performance of $Li_{1+x}Mn_{2-x}O_4$ spinels in terms of cyclability, columbic efficiency and charge-transfer resistance. They significantly reduce the charge-transfer resistance, lower the 1st cycle irreversible capacity to 6%, achieve a capacity retention between 85 and 90% after 380 cycles, with excellent columbic efficiency close to 99% and without compromising the specific charge at 5C cycling rate. The synthesis was carried out in a microwave-assisted hydrothermal at a low temperature of 140 °C for a short time of 5 min from aqueous based-solutions. SAXS and SEM confirmed the average size of the particles between (60 to 100 nm) and synchrotron X-ray diffraction validated the formation of highly crystalline Li-rich $Li_{1+x}Mn_{2-x}O_4$

cubic spinel phase. X-ray absorption spectroscopy analysis at the Co and Ni K- and L-edges verify that the dopants are within the $Li_{1+x}Mn_{2-x}O_4$ spinel structure and are inactive during cycling in the bulk and at the surface. From the XANES at Mn K-edge it was possible to monitor the Mn oxidation state in the bulk of the nanoparticles, and it was suggested that the insertion of the Li^+ ions is much easier in the nano-sized particles compared to the micron-sized, supported also by the higher columbic efficiency 94% during the 1st cycle. Mn L-edge spectra show that after long cycling the Mn oxidation state in the bulk differs from the one on the surface proposed to be caused by the surface Mn disproportion reaction. The cationic doping helps to mitigate the Mn dissolution with respect to the undoped nano-sized spinels as shown by the ICP measurements.

ASSOCIATED CONTENT

Supporting Information

Preliminary results from the microwave syntheses of Co- and Ni-doped spinels; particle size distribution (Monte Carlo fitting of the small-angle X-ray scattering data); lattice parameter *a* (powder X-ray diffraction and Rietveld refinements data analysis) of the samples as-synthesized and after different states of cycling states at C/10 rate; concentration of K^+ ions in the electrolyte; cycling performance of the synthesized material before removing the potassium birnessite phase contribution; oxidation state of Co and Ni (X-ray absorption spectra of Co and Ni L-edge and K-edge) and extended X-ray absorption fine structure (EXAFS) fitting for as-synthesized and collected in different cycling states at C/10 rate; oxidation state of Mn (X-ray absorption spectra of Mn K-edge) and EXAFS fitting for the as-synthesized and collected in different cycling states

at C/10 rate for the undoped and doped spinels; analysis for the Mn dissolution and values of OCP

for the electrodes before and after the 380th cycles.

AUTHOR INFORMATION

Corresponding Author

*Mario El Kazzi – Electrochemistry Laboratory, Paul Scherrer Institute, CH-5232 Villigen PSI, Switzerland; orcid.org/0000-0003-2975-0481; Email: mario.el-kazzi@psi.ch

Authors

Juliana B. Falqueto – [1] Electrochemistry Laboratory, Paul Scherrer Institute, CH-5232 Villigen PSI, Switzerland; [2] Federal University of São Carlos, Department of Chemistry, C.P. 676, 13560-970 São Carlos - SP, Brazil; orcid.org/0000-0001-5730-5014

Adam H. Clark – [3] Swiss Light Source, Paul Scherrer Institute, CH-5232 Villigen PSI, Switzerland; orcid.org/0000-0002-5478-9639

Aleš Štefančič – [1] Electrochemistry Laboratory, Paul Scherrer Institute, CH-5232 Villigen PSI, Switzerland; orcid.org/0000-0001-8491-2581

Glen J. Smales – [4] Bundesanstalt für Materialforschung und -prüfung (BAM), Unter den Eichen 87, DE-12205, Berlin, Germany; orcid.org/0000-0002-8654-9867

Carlos A. F. Vaz – [3] Swiss Light Source, Paul Scherrer Institute, CH-5232 Villigen PSI, Switzerland; orcid.org/0000-0002-6209-8918

Albert J. Schuler – [5] Bioenergy and Catalysis Laboratory, Paul Scherrer Institute, Forschungsstrasse 111, 5232 Villigen PSI, Switzerland

Nerilso Bocchi – [2] Federal University of São Carlos, Department of Chemistry, C.P. 676, 13560-970 São Carlos - SP, Brazil; orcid.org/0000-0002-9170-9925

Author Contributions

The manuscript was written through contributions of all authors. All authors have given approval to the final version of the manuscript.

Funding Sources

Notes

The authors declare no competing financial interest.

REFERENCES

(1)   Goodenough, J. B.; Park, K. The Li-Ion Rechargeable Battery: A Perspective. *Journal of American Chemical Society* **2013**, *135*, 1167–1176.

(2)   Thackeray, M. M.; Amine, K. Layered Li–Ni–Mn–Co Oxide Cathodes. *Nature Energy* **2021**, *6* (9), 933–933. https://doi.org/10.1038/s41560-021-00860-3.

(3)   Grey, C. P.; Tarascon, J. M. Sustainability and in Situ Monitoring in Battery Development. *Nature Materials* **2017**, *16* (1), 45–56. https://doi.org/10.1038/nmat4777.

(4)   Larcher, D.; Tarascon, J.-M. Towards Greener and More Sustainable Batteries for Electrical Energy Storage. *Nature Chemistry* **2014**, *7* (1), 19–29. https://doi.org/10.1038/nchem.2085.

(5)   Tarascon, J. M.; Guyomard, D. The $Li_{1+x}Mn_2O_4$/C Rocking-Chair System: A Review. *Electrochimica Acta* **1993**, *38* (9), 1221–1231. https://doi.org/10.1016/0013-4686(93)80053-3.

(6)   Liu, C.; Neale, Z. G.; Cao, G. Understanding Electrochemical Potentials of Cathode Materials in Rechargeable Batteries. *Materials Today* **2016**, *19* (2), 109–123. https://doi.org/10.1016/j.mattod.2015.10.009.

(7)   Chen, R.; Zhao, T.; Zhang, X.; Li, L.; Wu, F. Advanced Cathode Materials for Lithium-Ion Batteries Using Nanoarchitectonics. *Nanoscale Horizons* **2016**, *1* (6), 417–504. https://doi.org/10.1039/C6NH00016A.

(8)   Liu, T.; Dai, A.; Lu, J.; Yuan, Y.; Xiao, Y.; Yu, L.; Li, M.; Gim, J.; Ma, L.; Liu, J.; Zhan, C.; Li, L.; Zheng, J.; Ren, Y.; Wu, T.; Shahbazian-Yassar, R.; Wen, J.; Pan, F.; Amine, K. Correlation between Manganese Dissolution and Dynamic Phase Stability in Spinel-Based Lithium-Ion Battery. *Nature Communications* **2019**, *10* (1), 4721. https://doi.org/10.1038/s41467-019-12626-3.

(9)   Armstrong, M. J.; O'Dwyer, C.; Macklin, W. J.; Holmes, J. D. Evaluating the Performance of Nanostructured Materials as Lithium-Ion Battery Electrodes. *Nano Research* **2014**, *7* (1), 1–62. https://doi.org/10.1007/s12274-013-0375-x.

(10)   Ellis, B. L.; Lee, K. T.; Nazar, L. F. Positive Electrode Materials for Li-Ion and Li-Batteries. *Chemistry of Materials* **2010**, *22*, 691–714. https://doi.org/10.1021/cm902696j.

(11)   Velásquez, E. A.; Silva, D. P. B.; Falqueto, J. B.; Mejía-López, J.; Bocchi, N.; del Rio, R.; Mazo-Zuluaga, J.; Rocha-Filho, R. C.; Biaggio, S. R. Understanding the Loss of Electrochemical Activity of Nanosized $LiMn_2O_4$ Particles: A Combined Experimental and *Ab Initio* DFT Study. *Journal of Materials Chemistry A* **2018**, *6* (30), 14967–14974. https://doi.org/10.1039/C8TA02703J.

(12)   Bruce, P. G.; Scrosati, B.; Tarascon, J.-M. Nanomaterials for Rechargeable Lithium Batteries. *Angewandte Chemie International Edition* **2008**, *47* (16), 2930–2946. https://doi.org/10.1002/anie.200702505.

(13)   Zhuo, Z.; Olalde-Velasco, P.; Chin, T.; Battaglia, V.; Harris, S. J.; Pan, F.; Yang, W. Effect of Excess Lithium in $LiMn_2O_4$ and $Li_{1.15}Mn_{1.85}O_4$ Electrodes Revealed by Quantitative Analysis of Soft X-Ray Absorption Spectroscopy. *Applied Physics Letters* **2017**, *110* (9), 093902. https://doi.org/10.1063/1.4977502.

(14)   Raja, M. W.; Mahanty, S.; Basu, R. N. Influence of S and Ni Co-Doping on Structure, Band Gap and Electrochemical Properties of Lithium Manganese Oxide Synthesized by Soft Chemical Method. *Journal of Power Sources* **2009**, *192* (2), 618–626. https://doi.org/10.1016/J.JPOWSOUR.2009.03.040.
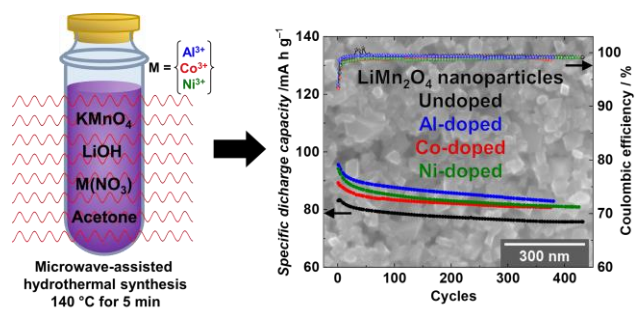
(15) Amaral, F. A.; Bocchi, N.; Brocenschi, R. F.; Biaggio, S. R.; Rocha-Filho, R. C. Structural and Electrochemical Properties of the Doped Spinels $Li_{1.05}M_{0.02}Mn_{1.98}O_{3.98}N_{0.02}$ ($M=Ga^{3+}$, Al^{3+}, or Co^{3+}; $N=S^{2-}$ or F^-) for Use as Cathod. *Journal of Power Sources* **2010**, *195* (10), 3293–3299. https://doi.org/10.1016/j.jpowsour.2009.12.002.

(16) Idemoto, Y.; Tejima, F.; Ishida, N.; Kitamura, N. Average, Electronic, and Local Structures of $LiMn_{2-x}Al_xO_4$ in Charge-Discharge Process by Neutron and Synchrotron X-Ray. *Journal of Power Sources* **2019**, *410–411*, 38–44. https://doi.org/10.1016/j.jpowsour.2018.10.067.

(17) Cai, Z.; Ma, Y.; Huang, X.; Yan, X.; Yu, Z.; Zhang, S.; Song, G.; Xu, Y.; Wen, C.; Yang, W. High Electrochemical Stability Al-Doped Spinel $LiMn_2O_4$ Cathode Material for Li-Ion Batteries. *Journal of Energy Storage* **2020**, *27*, 101036. https://doi.org/10.1016/j.est.2019.101036.

(18) Fang, D.-L.; Li, J.-C.; Liu, X.; Huang, P.-F.; Xu, T.-R.; Qian, M.-C.; Zheng, C.-H. Synthesis of a Co–Ni Doped $LiMn_2O_4$ Spinel Cathode Material for High-Power Li-Ion Batteries by a Sol–Gel Mediated Solid-State Route. *Journal of Alloys and Compounds* **2015**, *640*, 82–89. https://doi.org/10.1016/j.jallcom.2015.03.243.

(19) Zhu, Y.-J.; Chen, F. Microwave-Assisted Preparation of Inorganic Nanostructures in Liquid Phase. *Chemical Reviews* **2014**, *114*, 6462–6555. https://doi.org/10.1021/cr400366s.

(20) Schanche, J.-S. Microwave Synthesis Solutions from Personal Chemistry. *Molecular Diversity* **2003**, *7* (2–4), 291–298. https://doi.org/10.1023/B:MODI.0000006866.38392.f7.

(21) Liddle, B. J.; Collins, S. M.; Bartlett, B. M. A New One-Pot Hydrothermal Synthesis and Electrochemical Characterization of $Li_{1+x}Mn_{2-y}O_4$ Spinel Structured Compounds. *Energy & Environmental Science* **2010**, *3* (9), 1339. https://doi.org/10.1039/c0ee00059k.

(22) Meng, L.-Y.; Wang, B.; Ma, M.-G.; Lin, K.-L. The Progress of Microwave-Assisted Hydrothermal Method in the Synthesis of Functional Nanomaterials. *Materials Today Chemistry* **2016**, *1–2*, 63–83. https://doi.org/http://dx.doi.org/10.1016/j.mtchem.2016.11.003.

(23) Bilecka, I.; Niederberger, M. Microwave Chemistry for Inorganic Nanomaterials Synthesis. *Nanoscale* **2010**, *2* (8), 1358–1374. https://doi.org/10.1039/b9nr00377k.

(24) Meng, L.; Ushakova, E. v.; Zhou, Z.; Liu, E.; Li, D.; Zhou, D.; Tan, Z.; Qu, S.; Rogach, A. L. Microwave-Assisted *in Situ* Large Scale Synthesis of a Carbon Dots@g-C$_3$N$_4$ Composite Phosphor for White Light-Emitting Devices. *Materials Chemistry Frontiers* **2020**, *4* (2), 517–523. https://doi.org/10.1039/C9QM00659A.

(25) Glasnov, T. N.; Kappe, C. O. Microwave-Assisted Synthesis under Continuous-Flow Conditions. *Macromolecular Rapid Communications* **2007**, *28* (4), 395–410. https://doi.org/10.1002/marc.200600665.

(26) Ragupathy, P.; Vasan, H. N.; Munichandraiah, N. Microwave Driven Hydrothermal Synthesis of $LiMn_2O_4$ Nanoparticles as Cathode Material for Li-Ion Batteries. *Materials Chemistry and Physics* **2010**, *124* (1), 870–875. https://doi.org/10.1016/j.matchemphys.2010.08.014.

(27) Chen, K.; Donahoe, A. C.; Noh, Y. D.; Li, K.; Komarneni, S.; Xue, D. Conventional- and Microwave-Hydrothermal Synthesis of $LiMn_2O_4$: Effect of Synthesis on Electrochemical Energy Storage Performances. *Ceramics International* **2014**, *40* (2), 3155–3163. https://doi.org/10.1016/J.CERAMINT.2013.09.128.

(28) Liang, Y.; Bao, S.; Li, H. A Series of Spinel Phase Cathode Materials Prepared by a Simple Hydrothermal Process for Rechargeable Lithium Batteries. *Journal of Solid State Chemistry* **2006**, *179*, 2133–2140. https://doi.org/10.1016/j.jssc.2006.04.012.

(29) Smales, G. J.; Pauw, B. R. The MOUSE Project: A Meticulous Approach for Obtaining Traceable, Wide-Range X-Ray Scattering Information. *Journal of Instrumentation* **2021**, *16* (06), P06034. https://doi.org/10.1088/1748-0221/16/06/P06034.

(30) Pauw, B. R.; Smith, A. J.; Snow, T.; Terrill, N. J.; Thünemann, A. F. The Modular Small-Angle X-Ray Scattering Data Correction Sequence. *Journal of Applied Crystallography* **2017**, *50* (6), 1800–1811. https://doi.org/10.1107/S1600576717015096.

(31) Filik, J.; Ashton, A. W.; Chang, P. C. Y.; Chater, P. A.; Day, S. J.; Drakopoulos, M.; Gerring, M. W.; Hart, M. L.; Magdysyuk, O. v.; Michalik, S.; Smith, A.; Tang, C. C.; Terrill, N. J.; Wharmby, M. T.; Wilhelm, H. Processing Two-Dimensional X-Ray Diffraction and Small-Angle Scattering Data in DAWN 2. *Journal of Applied Crystallography* **2017**, *50* (3), 959–966. https://doi.org/10.1107/S1600576717004708.

(32) Bressler, I.; Pauw, B. R.; Thünemann, A. F. McSAS: Software for the Retrieval of Model Parameter Distributions from Scattering Patterns. *Journal of Applied Crystallography* **2015**, *48*, 962–969. https://doi.org/10.1107/S1600576715007347.

(33) Willmott, P. R.; Meister, D.; Leake, S. J.; Lange, M.; Bergamaschi, A.; Böge, M.; Calvi, M.; Cancellieri, C.; Casati, N.; Cervellino, A.; Chen, Q.; David, C.; Flechsig, U.; Gozzo, F.; Henrich, B.; Jäggi-Spielmann, S.; Jakob, B.; Kalichava, I.; Karvinen, P.; Krempasky, J.; Lüdeke, A.; Lüscher, R.; Maag, S.; Quitmann, C.; Reinle-Schmitt, M. L.; Schmidt, T.; Schmitt, B.; Streun, A.; Vartiainen, I.; Vitins, M.; Wang, X.; Wullschleger, R. The Materials Science Beamline Upgrade at the Swiss Light Source. *Journal of Synchrotron Radiation* **2013**, *20* (5), 667–682. https://doi.org/10.1107/S0909049513018475.

(34) Coelho, A. A. *TOPAS* and *TOPAS-Academic* : An Optimization Program Integrating Computer Algebra and Crystallographic Objects Written in C++. *Journal of Applied Crystallography* **2018**, *51* (1), 210–218. https://doi.org/10.1107/S1600576718000183.

(35) Müller, O.; Nachtegaal, M.; Just, J.; Lützenkirchen-Hecht, D.; Frahm, R. Quick-EXAFS Setup at the SuperXAS Beamline for in Situ X-Ray Absorption Spectroscopy with 10ms Time Resolution. In *Journal of Synchrotron Radiation*; International Union of Crystallography, 2016; Vol. 23, pp 260–266. https://doi.org/10.1107/S1600577515018007.

(36) Clark, A. H.; Imbao, J.; Frahm, R.; Nachtegaal, M. ProQEXAFS : A Highly Optimized Parallelized Rapid Processing Software for QEXAFS Data. *Journal of Synchrotron Radiation* **2020**, *27* (2), 551–557. https://doi.org/10.1107/S1600577519017053.

(37) Oikawa, K.; Kamiyama, T.; Izumi, F.; Nakazato, D.; Ikuta, H.; Wakihara, M. Neutron and X-Ray Powder Diffraction Studies of $LiMn_{2-y}Cr_yO_4$. *Journal of Solid State Chemistry* **1999**, *146* (2), 322–328. https://doi.org/10.1006/jssc.1999.8351.

(38) Holland, K. L.; Walker, J. R. Crystal Structure Modeling of a Highly Disordered Potassium Birnessite. *Clays and Clay Minerals* **1996**, *44* (6), 744–748. https://doi.org/10.1346/CCMN.1996.0440604.

(39) Xiao, W.; Xin, C.; Li, S.; Jie, J.; Gu, Y.; Zheng, J.; Pan, F. Insight into Fast Li Diffusion in Li-Excess Spinel Lithium Manganese Oxide. *Journal of Materials Chemistry A* **2018**, *6* (21), 9893–9898. https://doi.org/10.1039/C8TA01428K.

(40) Wu, H. M.; Tu, J. P.; Yuan, Y. F.; Chen, X. T.; Xiang, J. Y.; Zhao, X. B.; Cao, G. S. One-Step Synthesis $LiMn_2O_4$ Cathode by a Hydrothermal Method. *Journal of Power Sources* **2006**, *161* (2), 1260–1263. https://doi.org/10.1016/j.jpowsour.2006.05.011.

(41) Jiang, C.; Tang, Z.; Wang, S.; Zhang, Z. A Truncated Octahedral Spinel $LiMn_2O_4$ as High-Performance Cathode Material for Ultrafast and Long-Life Lithium-Ion Batteries. *Journal of Power Sources* **2017**, *357*, 144–148. https://doi.org/10.1016/j.jpowsour.2017.04.079.

(42) Kim, J.-S.; Kim, K.; Cho, W.; Shin, W. H.; Kanno, R.; Choi, J. W. A Truncated Manganese Spinel Cathode for Excellent Power and Lifetime in Lithium-Ion Batteries. *Nano Letters* **2012**, *12* (12), 6358–6365. https://doi.org/10.1021/nl303619s.

(43) Shannon, R. D. Revised Effective Ionic Radii and Systematic Studies of Interatomic Distances in Halides and Chalcogenides. *Acta Crystallographica Section A* **1976**, *32* (5), 751–767. https://doi.org/10.1107/S0567739476001551.

(44) Okubo, M.; Hosono, E.; Kim, J.; Enomoto, M.; Kojima, N.; Kudo, T.; Zhou, H.; Honma, I. Nanosize Effect on High-Rate Li-Ion Intercalation in $LiCoO_2$ Electrode. *J Am Chem Soc* **2007**, *129* (23), 7444–7452. https://doi.org/10.1021/ja0681927.

(45) Miyamoto, Y.; Kuroda, Y.; Uematsu, T.; Oshikawa, H.; Shibata, N.; Ikuhara, Y.; Suzuki, K.; Hibino, M.; Yamaguchi, K.; Mizuno, N. Synthesis of Ultrasmall Li–Mn Spinel Oxides Exhibiting Unusual Ion Exchange, Electrochemical and Catalytic Properties. *Scientific Reports* **2015**, *5* (1), 15011. https://doi.org/10.1038/srep15011.

(46) Wang, J.; Polleux, J.; Lim, J.; Dunn, B. Pseudocapacitive Contributions to Electrochemical Energy Storage in TiO_2 (Anatase) Nanoparticles. *The Journal of Physical Chemistry C* **2007**, *111* (40), 14925–14931. https://doi.org/10.1021/jp074464w.

(47) Okubo, M.; Kim, J.; Kudo, T.; Zhou, H.; Honma, I. Anisotropic Surface Effect on Electronic Structures and Electrochemical Properties of $LiCoO_2$. *The Journal of Physical Chemistry C* **2009**, *113* (34), 15337–15342. https://doi.org/10.1021/jp904877d.

(48) Abou-Rjeily, J.; Bezza, I.; Laziz, N. A.; Autret-Lambert, C.; Sougrati, M. T.; Ghamouss, F. High-Rate Cyclability and Stability of $LiMn_2O_4$ Cathode Materials for Lithium-Ion Batteries from Low-Cost Natural $\beta-MnO_2$. *Energy Storage Materials* **2020**, *26*, 423–432. https://doi.org/10.1016/j.ensm.2019.11.015.

(49)   Mosbah, A.; Verbaere, A.; Tournoux, M. Phases $Li_xMnO_2\lambda$ Rattachees Au Type Spinelle. *Materials Research Bulletin* **1983**, *18* (11), 1375–1381. https://doi.org/10.1016/0025-5408(83)90045-4.

(50)   Leanza, D.; Vaz, C. A. F.; Melinte, G.; Mu, X.; Novák, P.; el Kazzi, M. Revealing the Dual Surface Reactions on a HE-NCM Li-Ion Battery Cathode and Their Impact on the Surface Chemistry of the Counter Electrode. *ACS Applied Materials & Interfaces* **2019**, *11* (6), 6054–6065. https://doi.org/10.1021/acsami.8b19511.

(51)   Leanza, D.; Mirolo, M.; Vaz, C. A. F.; Novák, P.; el Kazzi, M. Surface Degradation and Chemical Electrolyte Oxidation Induced by the Oxygen Released from Layered Oxide Cathodes in Li−Ion Batteries. *Batteries & Supercaps* **2019**, *2* (5), 482–492. https://doi.org/10.1002/batt.201800126.

(52)   Iurilli, P.; Brivio, C.; Wood, V. On the Use of Electrochemical Impedance Spectroscopy to Characterize and Model the Aging Phenomena of Lithium-Ion Batteries: A Critical Review. *Journal of Power Sources* **2021**, *505*, 229860. https://doi.org/10.1016/j.jpowsour.2021.229860.

GRAPHICAL ABSTRACT

For Table of Contents Only